Supplementary Information

Highly efficient and durable solar thermal energy harvesting via scalable hierarchical coatings inspired by stony corals

Juan F. Torres,[1]✉ Kaoru Tsuda,[2]✉ Yasushi Murakami,[3] Yifan Guo,[1] Sahar Hosseini,[1] Charles-Alexis Asselineau,[1] Mahdiar Taheri,[1] Kurt Drewes,[4] Antonio Tricoli,[5,6] Wojciech Lipiński[1] and Joe Coventry[1]✉

[1] College of Engineering and Computer Science, The Australian National University, Canberra ACT, Australia

[2] Nano Frontier Technology, 3-10-6-105, Osaki, Shinagawa-ku, Tokyo, Japan

[3] Faculty of Textile Science and Technology, Shinshu University, 3-15-1, Tokida, Ueda, Nagano, Japan

[4] Vast Solar, Level 10, 17-19 Bridge St, Sydney, NSW 2000, Australia

[5] College of Science, The Australian National University, Canberra ACT, Australia

[6] Faculty of Engineering, The University of Sydney, Sydney, Australia

✉e-mails: felipe.torres@anu.edu.au, kaoru.tsuda@nano-frontier.com, joe.coventry@anu.edu.au

Supplementary Figures — referenced in article

Supplementary Notes

Supplementary Figures & Tables — referenced in notes

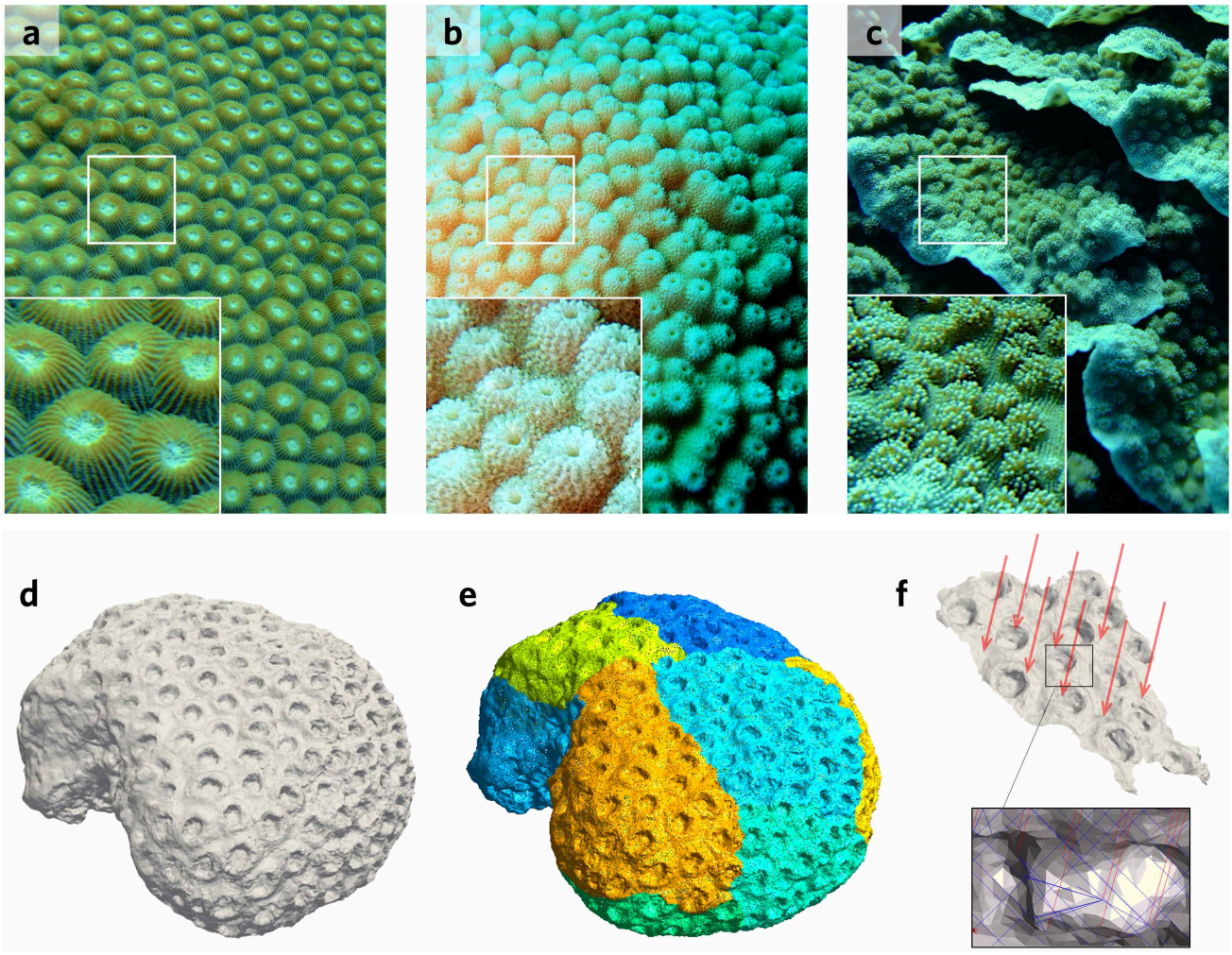

Fig. S1 | Coral morphology and surface preparation for ray-tracing simulations. Photos taken in Okinawa, Japan, of living stony corals with hierarchical morphology. Genus: **a**, *Montastraea*; **b**, *Astreopora*; and **c**, *Montipora*, from which our hierarchical high-temperature light-harvesting coating draws inspiration from. Polyps are ca. 7.5 mm in diameter. **d**, Three-dimensional scan of a modern specimen of the scleractinian coral: *Montastrea cavernosa*, from off Monroe County, Florida (source: collection of the Paleontological Research Institution, Ithaca, New York). Maximum dimension of specimen is approximately 11 cm. This is one of three coral morphologies that were analysed (**Fig. 1c**). **e**, Fragmentation of the stereolithography (STL) surface into sub-surfaces with less overall curvature. **f**, Depiction of ray-tracing simulation using a fragmented surface; 40,000 rays (in red) are emitted towards the surface; the inset depicts secondary diffuse reflections (blue rays). These multiple internal reflection are depicted in **Fig. 1b**.

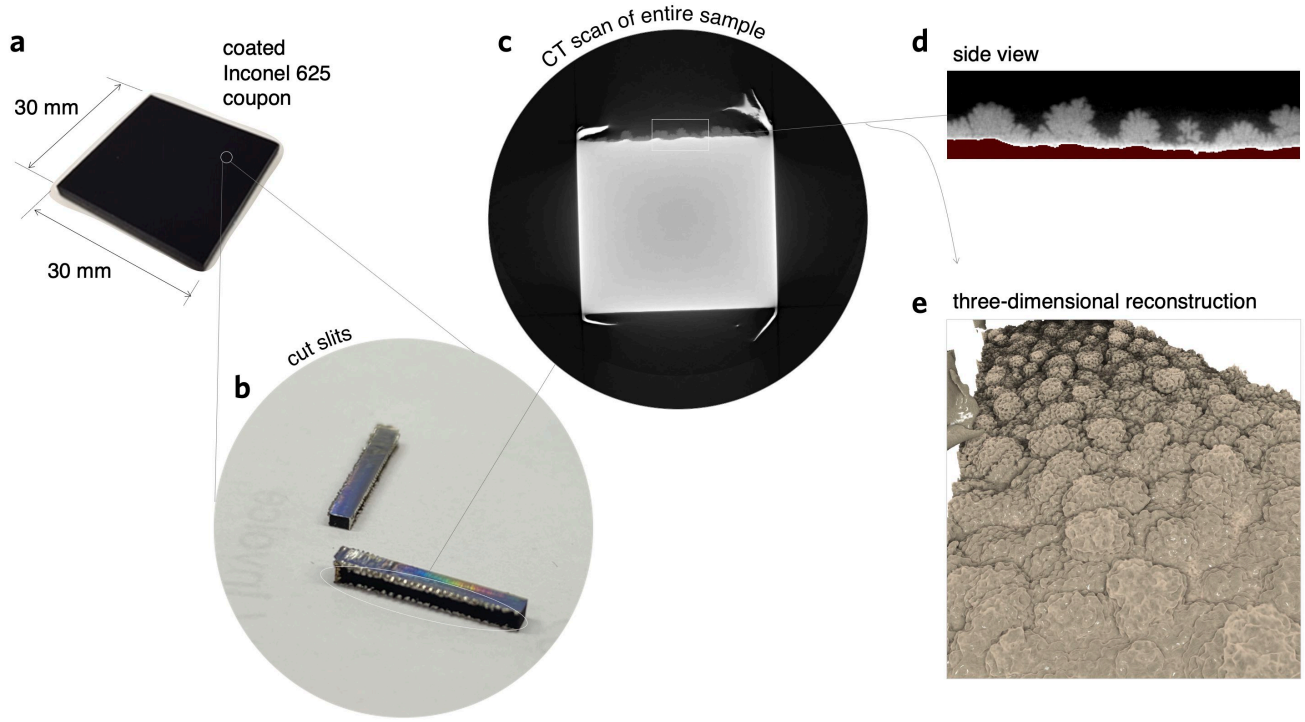

Fig. S2 | Computed tomography scan of macro- & micro-scale morphologies. a, Inconel 625 coupon (30 mm × 30 mm × 3 mm) coated with the coral-structured coating. **b**, Cut slits of ca. 3 mm wide and 15 mm long. **c**, Side view of the computed tomography (CT) scan of the entire sample; the region in light grey corresponds to the metallic substrate. **d**, Side view focused on the coral-structured morphology. **e**, Three-dimensional reconstruction of the CT scan, confirming the macro-scale protrusions and open micropore morphologies of the coating.

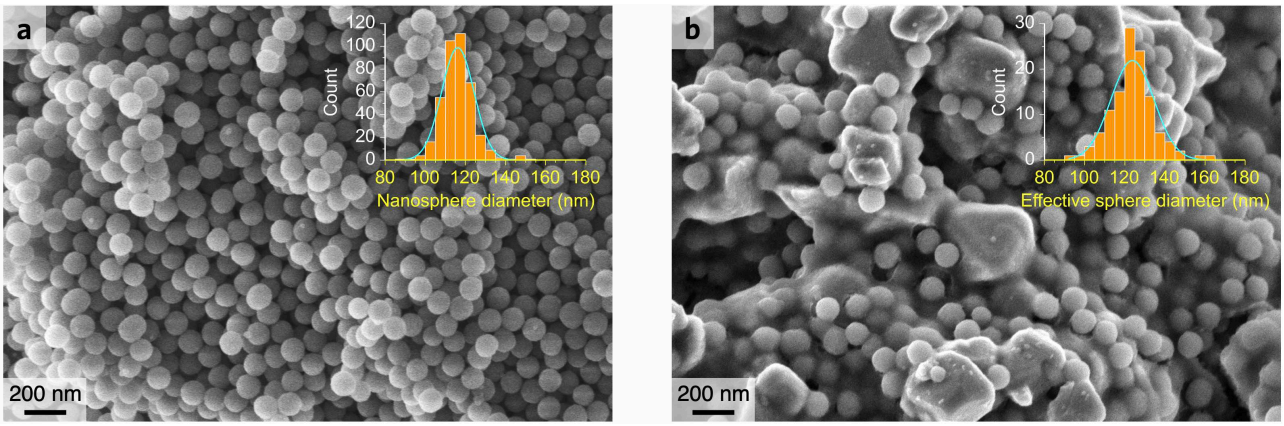

Fig. S3 | Quantitative analysis of nano-scale morphology. a, SEM image showing the nanospheres before mixing in top layer solution. The histogram plots the count of nanosphere diameter (size), i.e. before top layer preparation. The mean particle diameter is 116.2 nm with standard deviation of 8.1 nm. **b**, SEM image showing the nano-scale morphology on the coral-structured coating (same as **Fig. 2a.1**). The histogram plots the count of effective sphere diameter, i.e. after top layer deposition. The mean particle diameter is 124 nm with standard deviation of 11 nm.

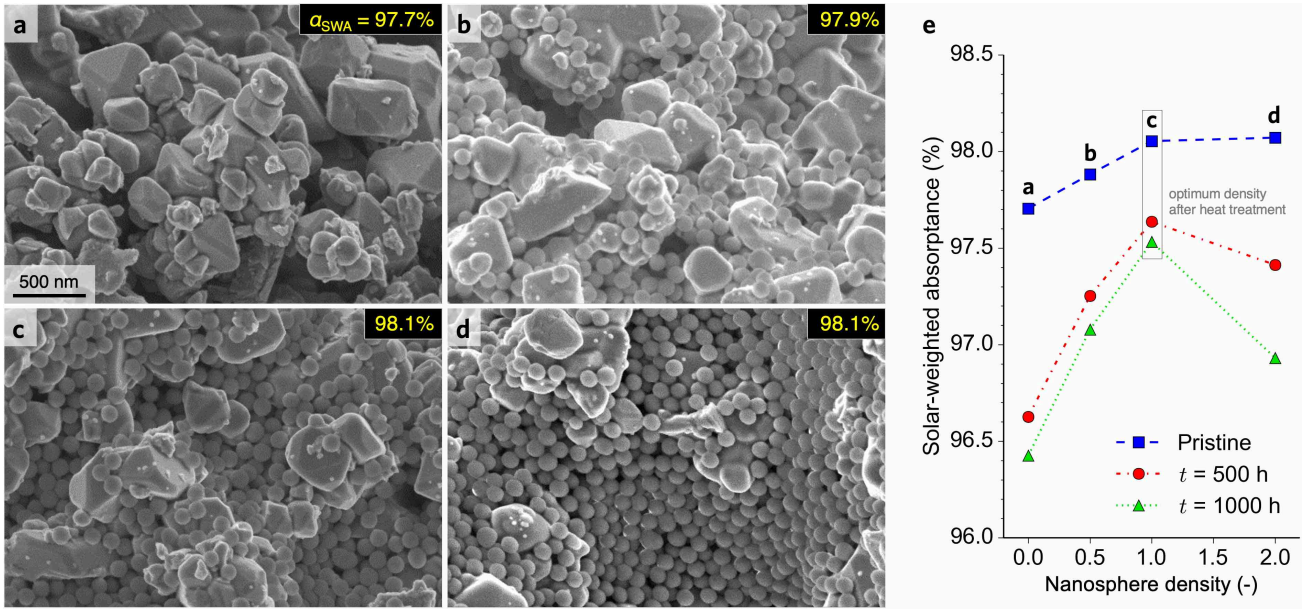

Fig. S4 | Tuneable nano-scale morphology by adjusting nanosphere density. High magnification SEM images (**a**–**d**) for the pristine coral-structured coating without top layer and with top layer having different number density of nanospheres, due to different concentration of nanospheres in the top layer solution, together with the corresponding solar-weighted absorptance. **a**, Absorption layer morphology without nanospheres (same scale bar for all SEM images). **b**, Morphology after adding the top layer with half of the nanosphere density that was found to be optimum, which is determined after ageing at 900°C for up to 1000 h. **c**, Morphology with optimum nanosphere density. **d**, Morphology with top layer having double the density of the optimum value. The value of the solar-weighted absorptance is indicated in each SEM image for the pristine condition. **e**, Solar-weighted absorptance as a function of the nanosphere number density (relative to the optimum value) for pristine condition and after ageing at 900°C for 500 h (same as inset in **Fig. 3e**) and 1000 h.

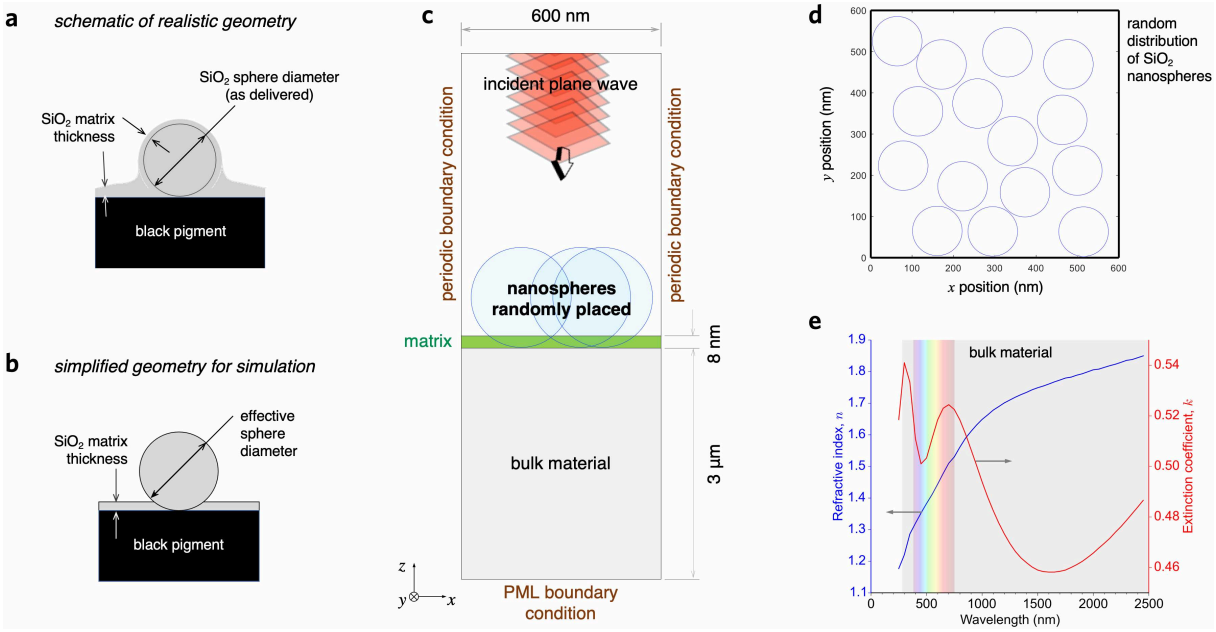

Fig. S5 | Computational electromagnetics model of the top layer. Schematic of a realistic morphology around a deposited nanosphere in the top layer. **a**, The bottom section of the nanospheres overlaps with the matrix, which also increases the sphere diameter by ca. twice the matrix thickness. **b**, Simplification of nano-scale morphology comprising a sphere and matrix for the computational electromagnetics simulation. The effective nanosphere diameter of 124 nm was directly measured (**Fig. S3b**), and the matrix thickness was estimated. **c**, Side view of simulation setups: the periodic boundary conditions are set along *z* on the lateral planes *xz* and *yz*; the perfectly matched layer (PML) boundary condition is set at the bottom and top *xy* plane boundaries. The thicknesses of matrix and bulk material are set to 8 nm and 3 µm, respectively, the latter ensuring that all the energy is absorbed before reaching the bottom. The mesh size is 2 nm. **d**, Top view of 15 randomly distributed nanosphere array on a 0.36 μm^2 area. **e**, Complex refractive index of the bulk material used in the FDTD simulations.

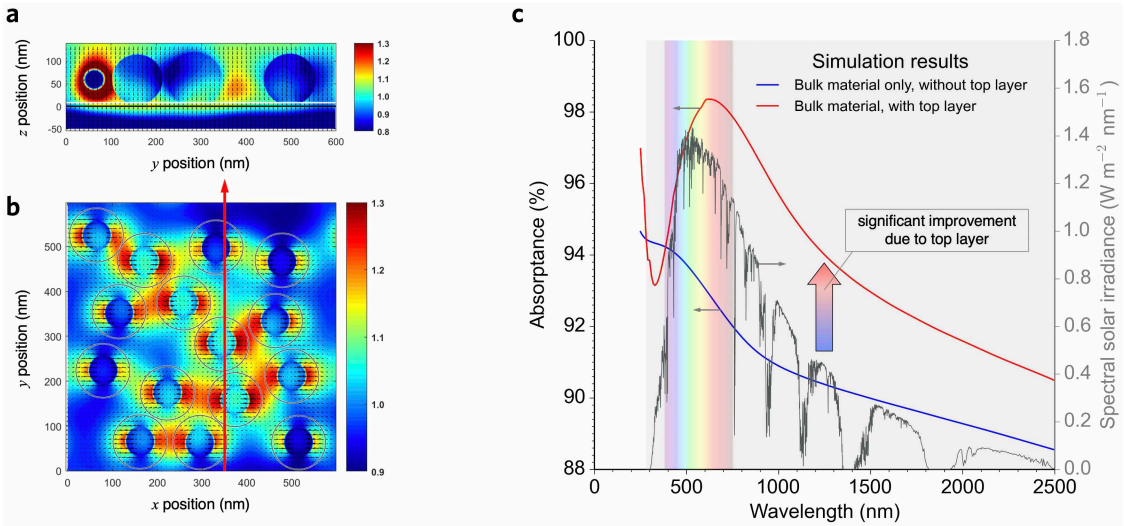

Fig. S6 | Effect of nanospheres: Poynting-vector distribution and spectral absorptance. Finite-difference time-domain (FDTD) simulation results for a top layer having 124 nm silica nanospheres and a surface area coverage ratio of 47%. **a**, Normalised light intensity (normalised against the incident power) from a cross-section side view at *x* = 350 nm and wavelength of 550 nm. **b**, Forward scattered light underneath the nanospheres (same as **Fig. 2b.1**). High-intensity regions between the spheres are caused by a resonance effect. **c**, Spectral absorptance of a flat bulk material with and without the top layer. The results are dependent on the nanosphere size, density, underlying coating complex index of refraction and underlying morphology.

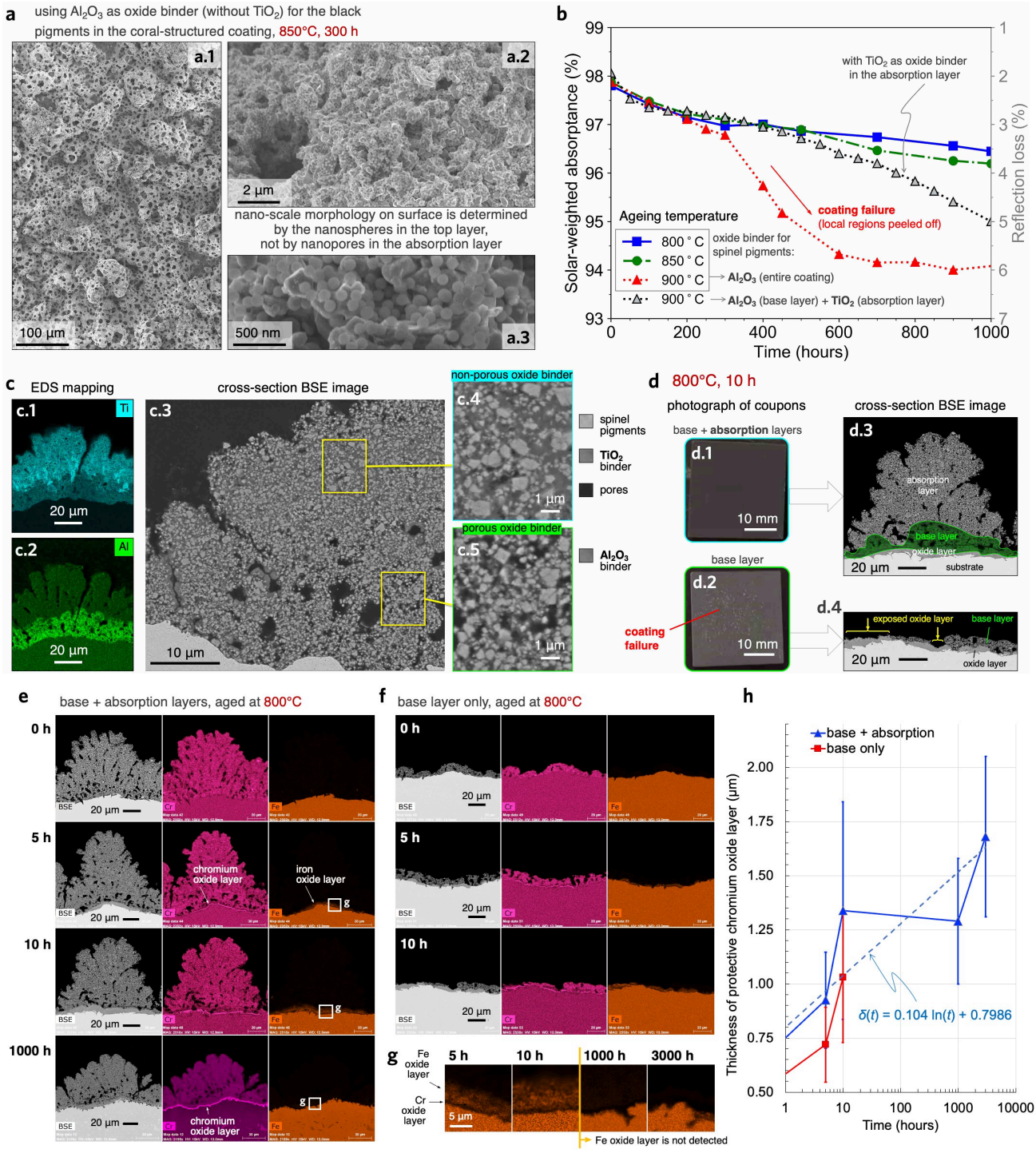

Fig. S7 | Enhanced durability of coral-structured coating with titania binder in absorption layer. Coatings on stainless steel 316L. **a**, SEM images of a modified coral-structured coating in which alumina was used as oxide binder in the entire coral-structured coating, without titania. **b**, Solar-weighted absorptance of the coating in panel (**a**) (coloured lines) aged up to 1000 h at 800°C (□), 850°C (○), and 900°C (△), and the coral-structured coating (black line) that uses titania as oxide binder in the absorption layer when aged at 900°C (reported in **Fig. S12b**). The titania in the absorption layer significantly improved durability. **c**, Cross-section analysis of the proposed coral-structured coating: elemental mapping showing Ti and Al in absorption (**c.1**) base (**c.2**) layers, respectively; high-resolution BSE image (**c.3**) showing details of the low porosity (or high density) in the absorption layer binder (**c.4**) and relatively high porosity (or low density) in the base layer binder (**c.5**). **d**, Durability improvement observed when adding the absorption layer (with titania) on base layer (with alumina), which is a coating that does not fail when aged at 800°C for 10 h (**d.1**). In contrast, the coating

comprised of only the base layer failed (**d.2**). The corresponding cross-section BSE images showing the structural durability of our coating (**d.1**, **d.3**), i.e. the morphology of the coating is not affected by the oxide layer growth at the coating–substrate boundary. It is worth noting that we also tested the titania binder in both base and absorption layers (without alumina), but the adhesion of titania onto the substrate was weak and failure was observed (not shown here). **e**, Cross-section images of BSE and elemental mapping for Cr and Fe for the coral-structured coating in pristine condition and when aged at 800°C for 5, 10, and 1000 h, showing the oxide layer growth at the interface between boundary and substrate. Two distinct oxide layers were observed: a Cr oxide layer growing underneath a relatively thicker Fe oxide layer, i.e. corresponding to protective and non-protective regions, respectively.[1] **f**, The same as in panel (**e**) but for a coating with only base layer aged up to 10 h, at which point coating failure was observed, as per photograph in panel (**d.2**). **g**, Large-magnification EDS images focusing on the Fe oxide layer in the coral-structured coating; magnified regions are shown in panel (**e**). In the initial stages (≤10 h), the Fe oxide layer is thicker than the Cr oxide layer, which is a result of a faster cation diffusion[2] for Fe than for Cr at 800°C. However, the Fe oxide layer was not clearly observed at ≥1000 h, suggesting that the Cr oxide layer blocked Fe cations from further diffusing from the substrate. The Fe cations that initially diffused could have further diffused into the absorption layer and hence were not detected at ≥1000 h. **h**, The thickness of the Cr oxide layer as a function of time when aged at 800°C. The error bars indicate the variance by denoting the ± standard deviation. Interestingly, the coating with base and absorption layers yields a Cr oxide layer that is approximately 25% thicker than the coating that only has the base layer. This result could be attributed to the presence of Cr in the spinel pigments, which are more abundant when having the absorption layer. We also conducted tests for bare substrates without coating (not shown here) and found that the Cr oxide layer was even thinner than the case with base layer only, supporting the conjecture that the Cr-based spinels in the coating contribute to the growth of the protective Cr oxide layer. This could be the reason why spinels that have Fe, instead of Cr, are less durable (see results in **Fig. S19**). A thicker Cr oxide layer has two potential benefits: reduction in Fe oxide layer growth, and reduction in tensile thermal stresses. Hence, an absorption layer with Cr-based spinels firmly bonded with a highly dense titania binder contributes greatly to the durability of our coral-structured coating, even on stainless steel which is known to be less corrosion-resistant than nickel-based alloys at elevated temperatures.

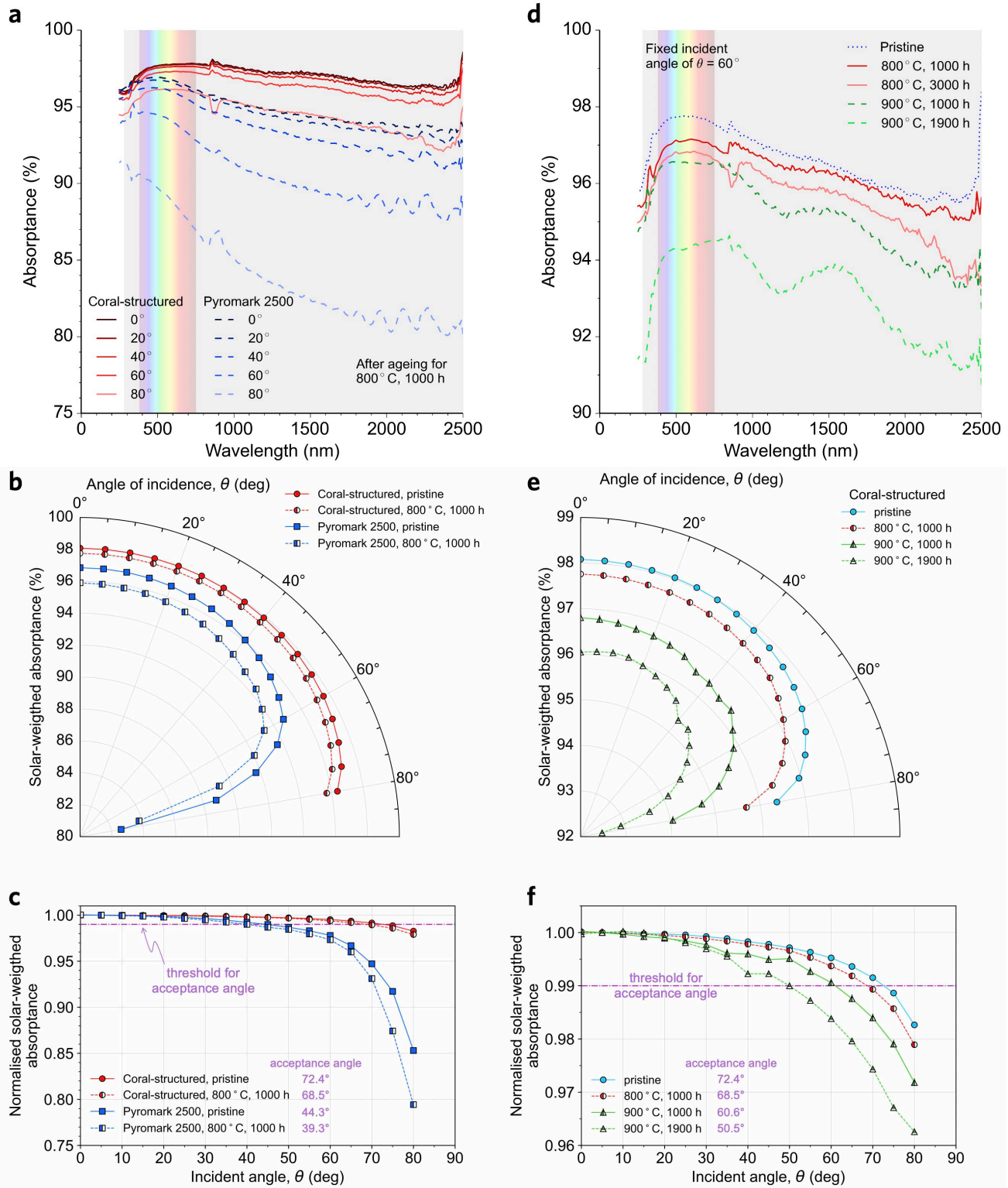

Fig. S8 | Angular absorptance for the coral-structured coating and Pyromark. a, Spectral absorptance of the proposed coral-structured coating (solid lines) and Pyromark 2500® (dashed lines) after ageing at 800°C for 1000 h for five angles of incidence: 0°, 20°, 40°, 60°, and 80°. **b**, Solar-weighted absorptance as a function of the angle of incidence for the proposed coral-structured coating (red circles) and Pyromark (blue squares) both on Inconel 625, before and after ageing at 800°C for 1000 h (solid and half-solid markers, respectively). **c**, Data in panel **a** normalised against the normal incidence value, i.e. when $\theta = 0°$; in this study, the acceptance angle is defined as the angle for which the normalised solar-weighted absorptance becomes 0.99. The acceptance angle

in each case is indicated in the legend. **d**, Spectral absorptance of the coral-structured coating at a fixed angle of incidence of 60° for the pristine coating (blue) and when aged at 800°C (red) and 900°C (green) each for two ageing times. **e**, Solar-weighted absorptance of the coral-structured coating as a function of the angle of incidence for a pristine coating (blue) and when aged at 800°C (red) and 900°C (green). **f**, Corresponding normalised solar-weighted absorptance. The acceptance angle is reduced as the temperature and ageing time are increased. Importantly, the coral-structured coating when aged at 900°C for 1900 h was better than Pyromark when aged at 800°C for 1000 h, despite the former having larger temperature value (+100°C) and ageing time (+900 h). The superiority of the proposed coral-structured coating over the state-of-the-art was confirmed for both solar-weighted absorptance at near-normal incidence and acceptance angle, i.e. our coatings had an acceptance angle of 50.5° when aged at 900°C for 1900 h, whereas that of Pyromark was 39.3° when aged at 800°C for 1000 h.

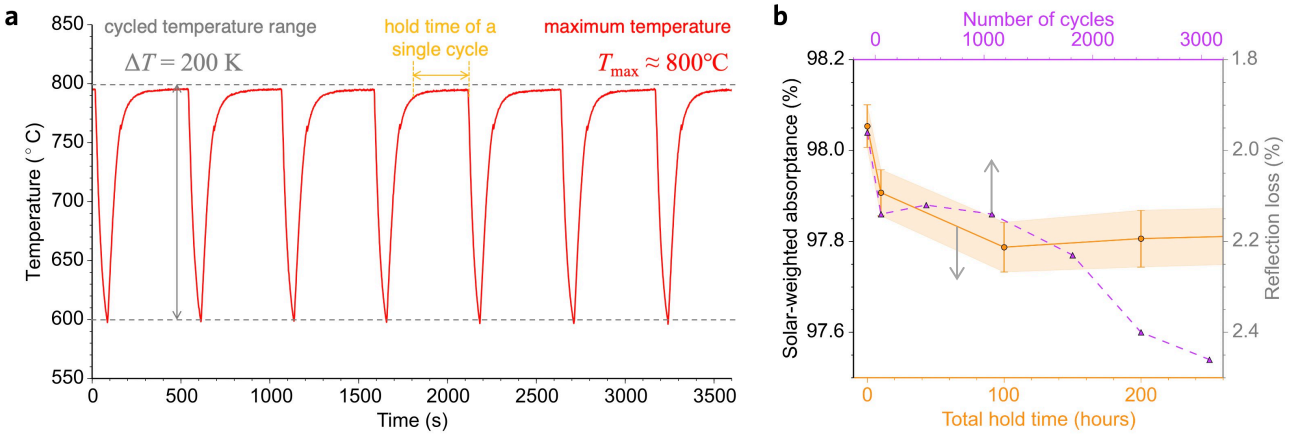

Fig. S9 | Extensive cycle-and-hold thermal cycling tests: pattern and results. a, Cycling pattern during a cycle-and-hold experiment. The one-hour data contains ca. 7.5 cycles; more than 3000 cycles were applied in total, with the experimental setup described in [3]; the temperature is measured with a thermocouple embedded in the substrate 0.5 mm below the coating surface. **b**, Solar-weighted absorptance as a function of total hold time (isothermal ageing; ○) and number of cycles (thermal cycling; △); same data as that in the inset of **Fig. 3b**.

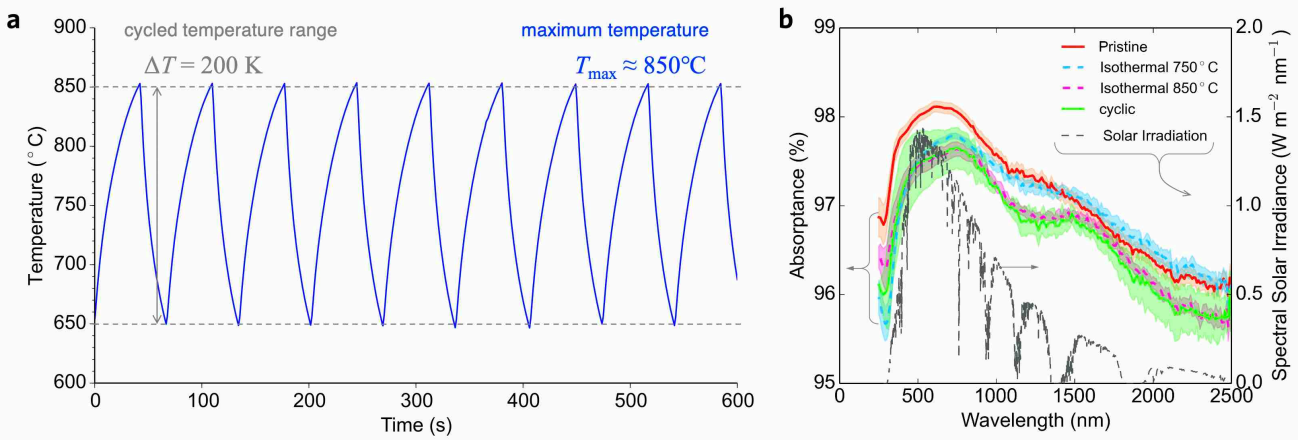

Fig. S10 | Extensive rapid thermal cycling tests: pattern and results. a, Thermal cycling pattern in a rapid cycling experiment, 10-minute data containing ca. 8.8 cycles; The total time for this test was 90 h with more than 4500 cycles. **b**, Spectral absorptance results after rapid cycling with the thermal cycling pattern in panel (**a**), as well as after isothermal ageing with the same duration of 90 h. The shaded region denotes the standard deviation of the spectral absorptance, as multiple samples were measured to confirm the repeatability.

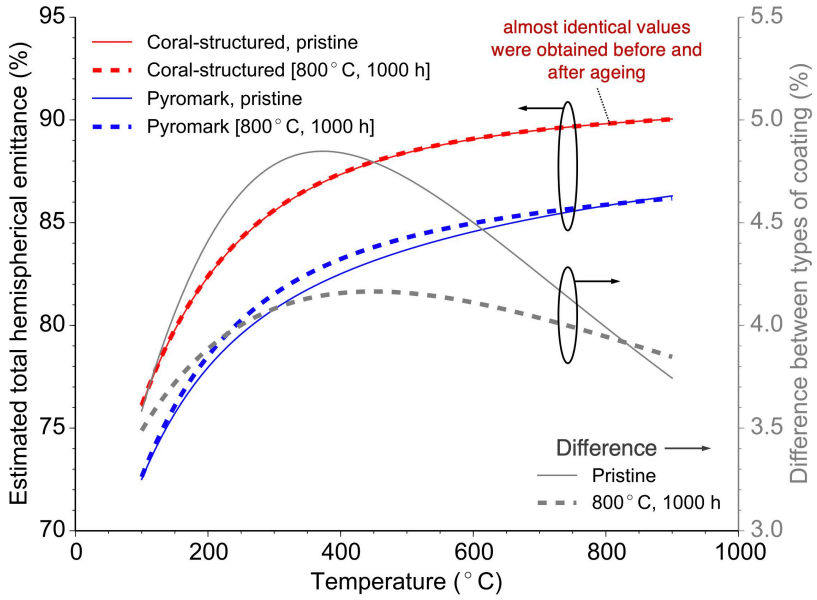

Fig. S11 | Estimated total hemispherical emittance as a function of temperature. Total hemispherical emittance (left axis) versus temperature for two coatings: our coral-structured coating (red) and Pyromark 2500® (blue), both on Inconel 625 before ageing (thin solid lines) and after ageing at 800°C for 1000 h (thick dashed lines). The difference between both coatings is less than 5% (grey lines; right axis). As indicted in the Methods, the spectral directional emittance at 17° is first measured at room temperature. We approximate this emittance to be the spectral near-normal emittance (**Fig. 3d**) because the spectral directional absorptance (and hence spectral directional emittance based on Kirchhoff's law) has a weak dependence with the angle of incidence for angles less than the acceptance angle of 72.4° (**Fig. S8**). The total hemispherical emittance is estimated from the near-normal emittance value and the ratio of normal emittance to total hemispherical emittance of 0.94 (taken from Ref. [4] for Pyromark). A more sophisticated measurement (as that in Ref. [5]) would be required to obtain an accurate measurement of the total hemispherical emittance for our coating. Nonetheless, the estimate values indicate that the total hemispherical emittance for the coral-structured coating was virtually unchanged after thermal annealing, whereas it increased for Pyromark at most temperature values. This result shows that our coatings is more optically stable than Pyromark in the infrared range.

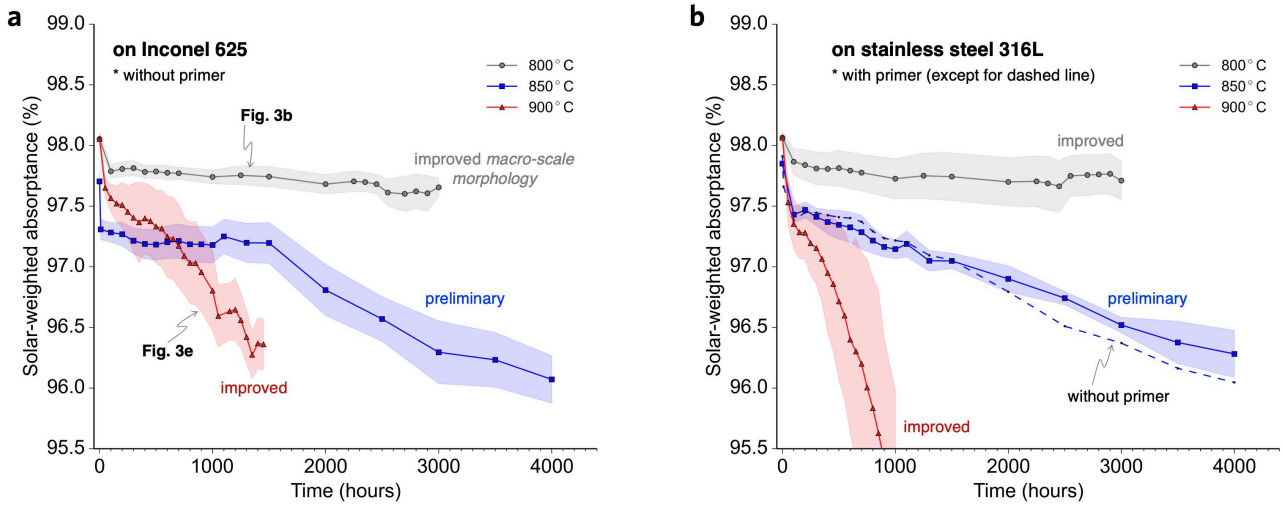

Fig. S12 | Long-term isothermal ageing of our coral-structured coating on two substrates. Two substrates were used for long-term testing of the coral-structured coatings for temperatures of 800, 850, and 900°C, up to 4000 h. **a**, Results for Inconel 625 (without primer). **b**, Results for stainless steel 316L (without primer; except for dashed line).

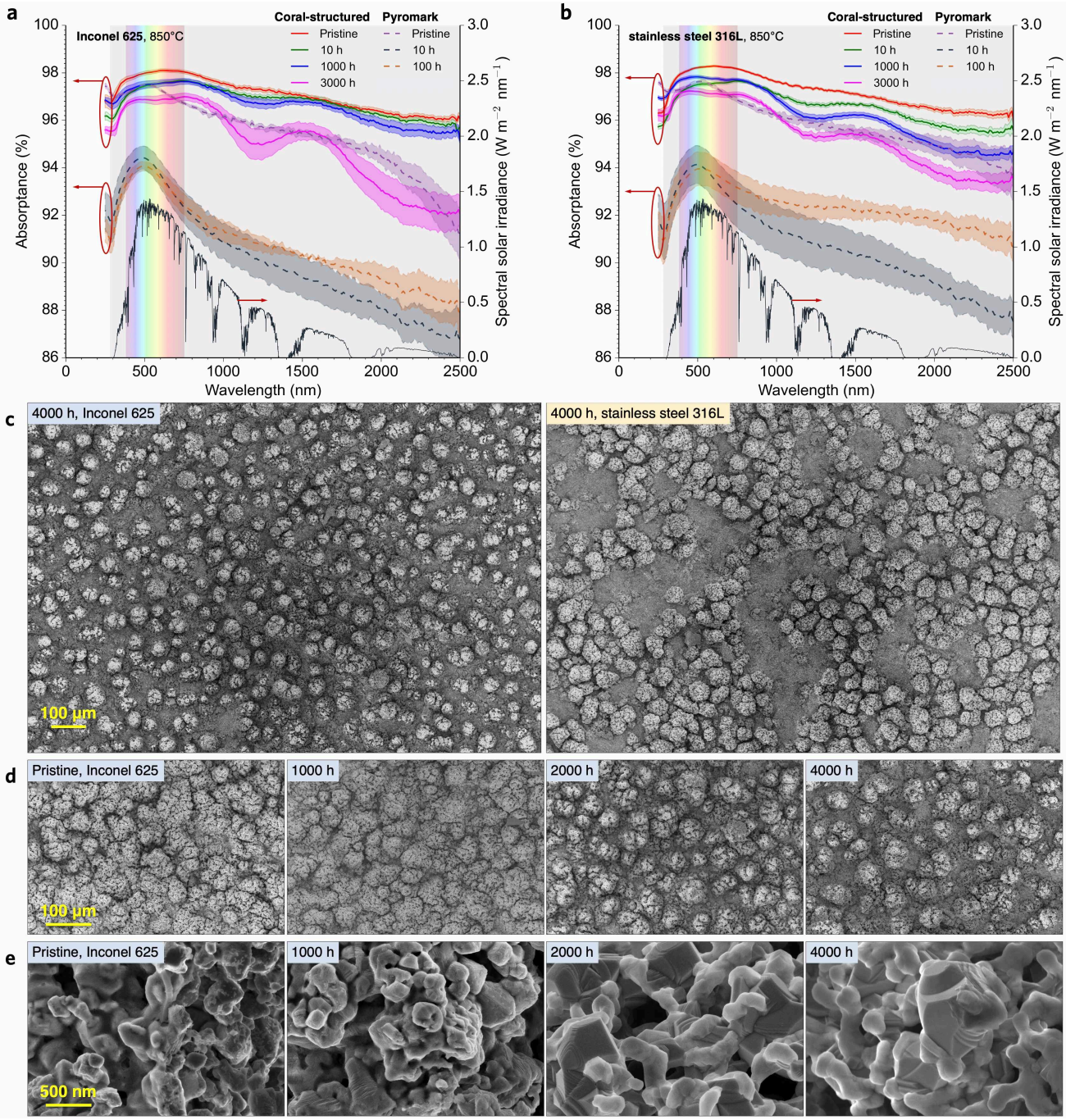

Fig. S13 | Absorptance and morphology of our coral-structured coating after ageing at 850°C. a, Spectral absorptance for our coral-structured coating (preliminary morphology) in pristine condition and after ageing at 850°C for 10, 1000 and 3000 h; Pyromark coating in pristine condition and after ageing for 10 and 100 h is included as reference. The absorptance of this Pyromark coating is not as high as that reported in the manuscript in **Figs. 3b**, **e** (aged at 800 and 900°C, respectively), which was improved by modifying the substrate roughness, coating thickness, and curing temperature.[6] **b**, The same as in panel (**a**) but for stainless steel 316L as the substrate. **c**, Low-magnification SEM images for our coating on Inconel 625 (left) and stainless steel 316L (right) after ageing at 850°C for 4000 h; rather large peeled off areas are observed in the latter. **d**, Low-magnification SEM images for the preliminary coral-structured coating on Inconel 625 in pristine condition and when aged for 1000, 2000 and 3000 h (from left to right). **e**, High-magnification SEM images for the same samples as those in panel (**d**). Note that the nano-scale morphology of the preliminary coating does not have the well-defined silica nanospheres, but rather particles with irregular shape. A well-defined nanosphere shape was incorporated in the improved coral-structured coating (**Figs. S3, S4**).

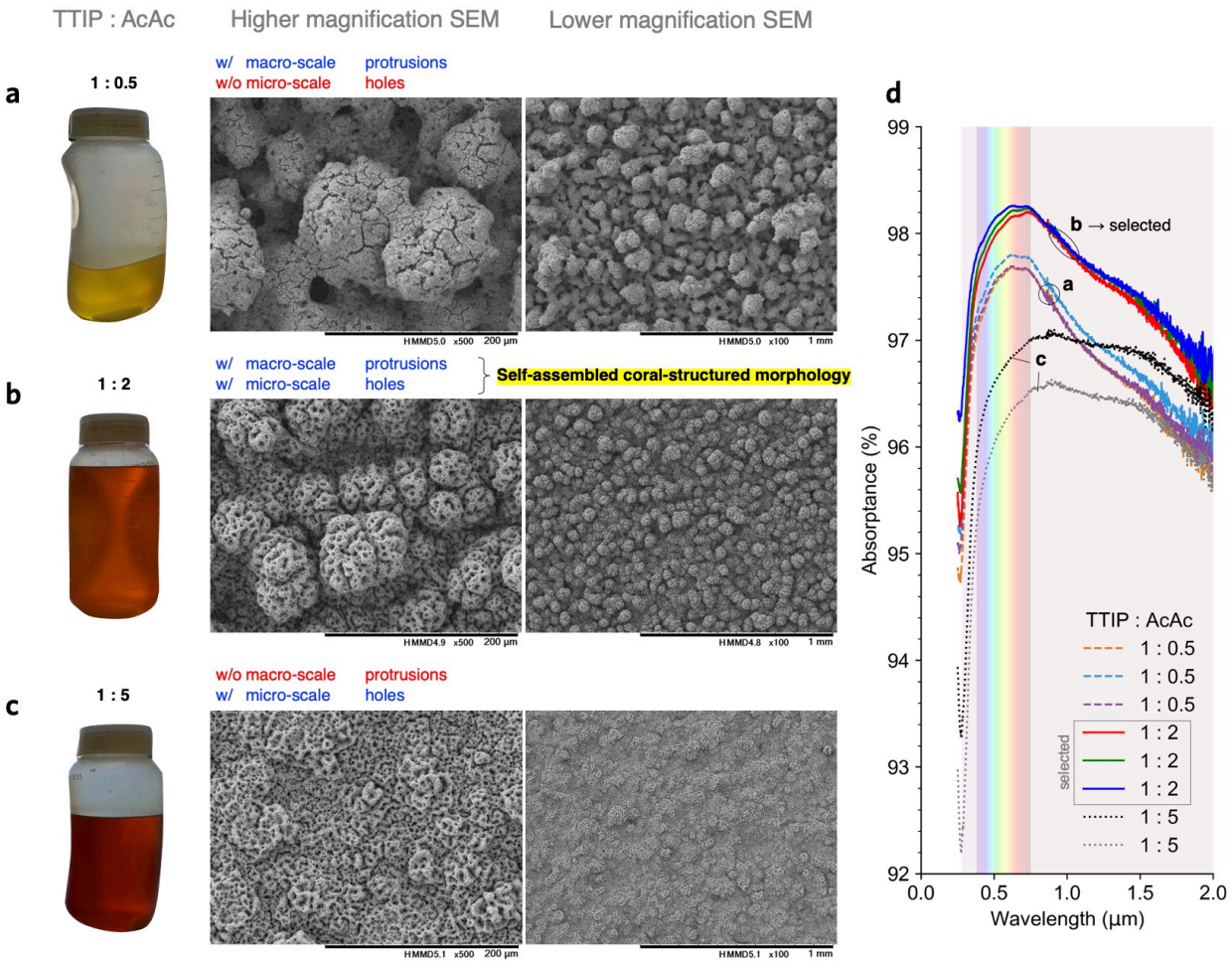

Fig. S14 | Tuneable macro- & micro-scale morphologies by adjusting TTIP : AcAc ratio. Both macro- and micro-scale morphologies can be tuned by varying the ratio of the titanium precursor (titanium isopropoxide, or TTIP) to acetylacetone (AcAc); here, three representative examples are shown, all of which have the top layer (i.e. nano-scale morphology). **a**, Absorption layer produced with an absorption solution of TTIP : AcAc = 1 : 0.5, which corresponds to a small amount of AcAc relative to TTIP; photograph of the solution (left; before mixing with spinel pigments) and higher/lower magnification SEM images showing a clear macro-scale morphology without micro-holes. **b**, Absorption layer produced with a solution having TTIP : AcAc = 1 : 2, which corresponds to the selected (nearly optimum) ratio used in the coatings reported in the main manuscript; photograph of the solution with SEM images showing the presence of both macro-scale protrusions and open micropores, which are key characteristics of the coral-structured morphology developed in this study. **c**, Solution and corresponding coating when using TTIP : AcAc = 1 : 5, corresponding to a large amount of AcAc relative to TTIP; SEM images show the lack of macro-scale protrusions yet with open micropores. **d**, Spectral absorptance for coatings produced with the TTIP : AcAc ratio specified in panels **a**–**c**. The ratio TTIP : AcAc = 1 : 2 was found to produce the largest absorption.

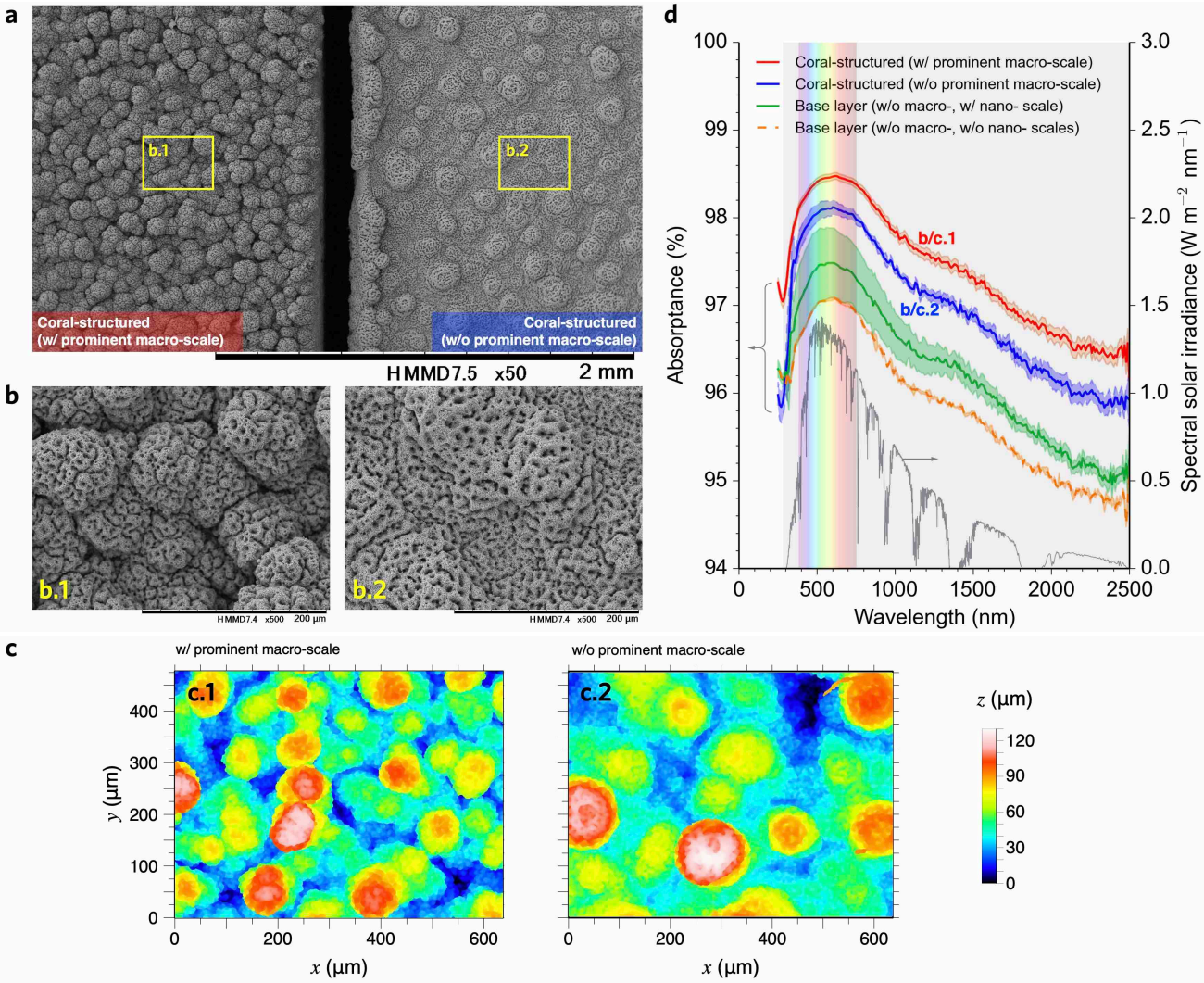

Fig. S15 | Tuneable macro-scale morphology by adjusting spray liquid pressure. These results demonstrate how the macro-scale morphology (protrusions) can be tuned with the spray liquid pressure. **a**, Low-magnification SEM image showing two samples next to each other: one is the improved coral-structured coating (left) and the other is the coral-structure coating that is rather flat (right), i.e. with less and smaller protrusions; this morphology is increased by increasing the liquid pressure when depositing the absorption solution. **b**, Higher magnification SEM images of the improved coral-structured coating (**b.1**) and the rather flat coating (**b.2**). **c**, Confocal microscope measurement of topography. **d**, Spectral absorptance for the improved coral-structured coating (red), coral-structured coating that is rather flat (blue), base layer with top layer (green), and bare base layer (orange); the solid lines correspond to samples with optimised top layer (see **Fig. S4**), whereas the dashed line is for the base layer without the top layer.

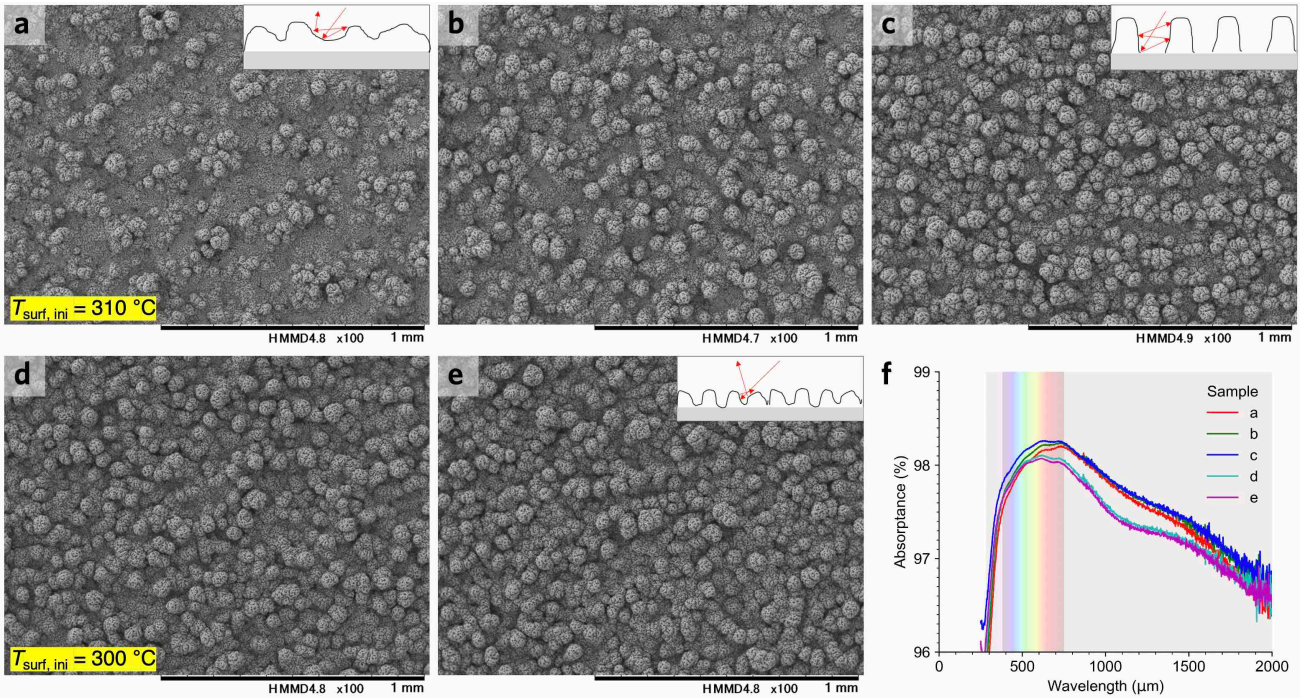

Fig. S16 | Tuneable number density of protrusions by adjusting the substrate temperature. SEM images (**a**–**e**) showing a varying number density in macro-scale protrusions as the substrate temperature (during deposition) is decreased, with corresponding spectral absorptance (**f**) for these morphologies. The absorption layer for all coatings was prepared with the same number of passes. First, the surface temperature of the substrate was set to $T_{suf, ini}$. Then, in the first spray round, consecutive spray passes were applied. Next, we waited for a hold time of Δt_{hold} for the surface temperature to stabilise. Then, in the second spray round, the absorption solution was applied several times. Finally, the top layer with optimum nanosphere density was applied. **a**–**c**, $T_{suf, ini}$ = 310°C; the evaporation of some of the absorption solution reduced the surface temperature to ca. 295°C. **d**–**e**, $T_{suf, ini}$ = 300°C; the evaporation of some of the absorption solution reduced the surface temperature to ca. 278°C. The hold time for the second batch (**d**–**e**) was 2/3 of the first batch (**a**–**c**), so the temperature of the second round did not reach $T_{suf, ini}$ = 300°C. For a given batch, samples were produced one after the other, so the initial temperature is thought to slightly decrease gradually, producing the slight differences in spectral absorptance within the same batch.

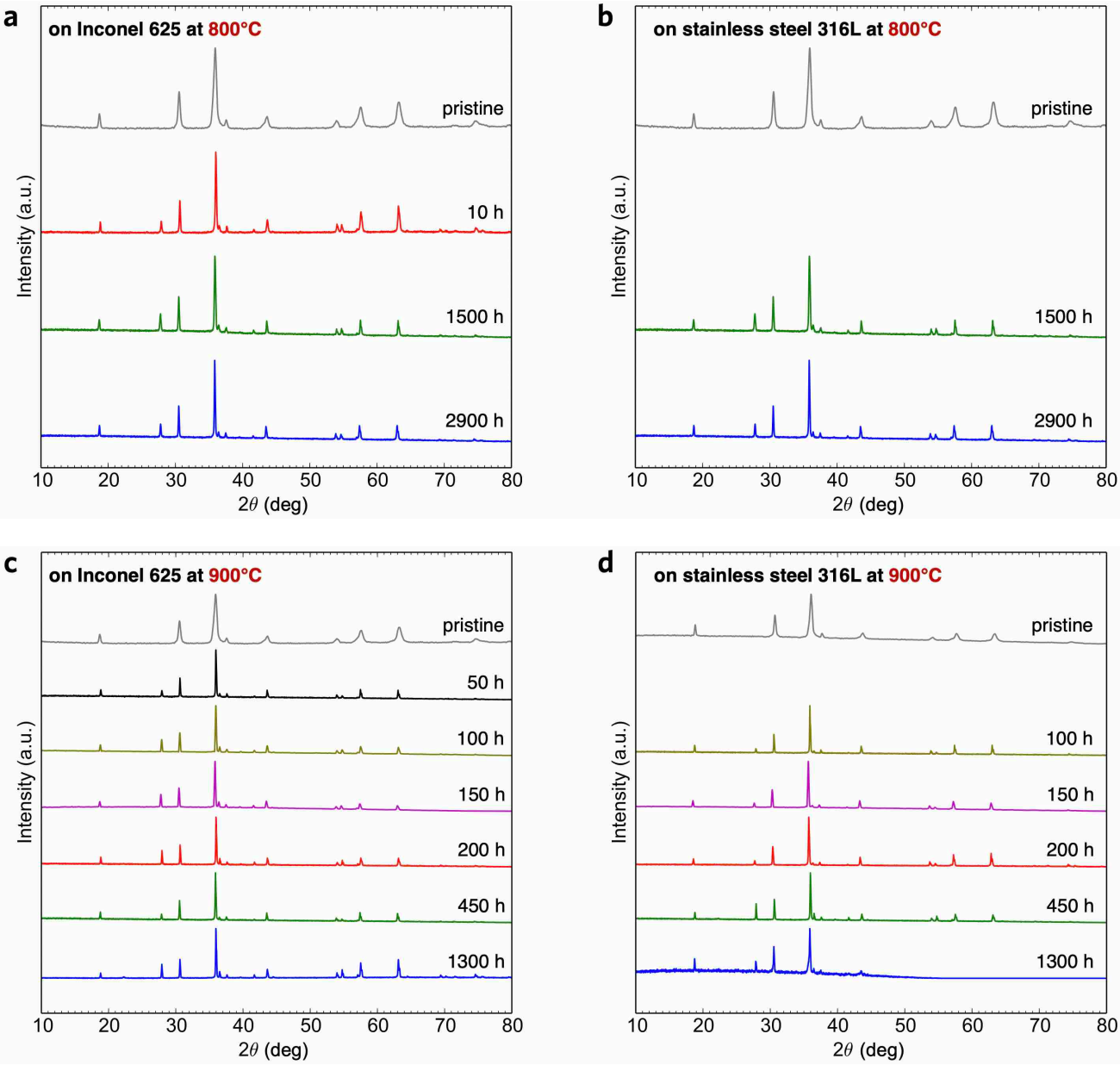

Fig. S17 | XRD patterns of the coral-structured coating after ageing at 800 and 900°C. XRD measurements for the coral-structured coating after annealing at 800°C (top; **a**, **b**) and 900°C (bottom; **c**, **d**) for a long-time period on Inconel 625 (left; **a**, **c**) and stainless steel 316L (right; **b**, **d**). These measurements indicate the coating materials are highly stable, the exception being for the coating deposited on stainless steel 316L and aged at 900°C for 1300 h (**d**), which is consistent with observed large peeled off regions.

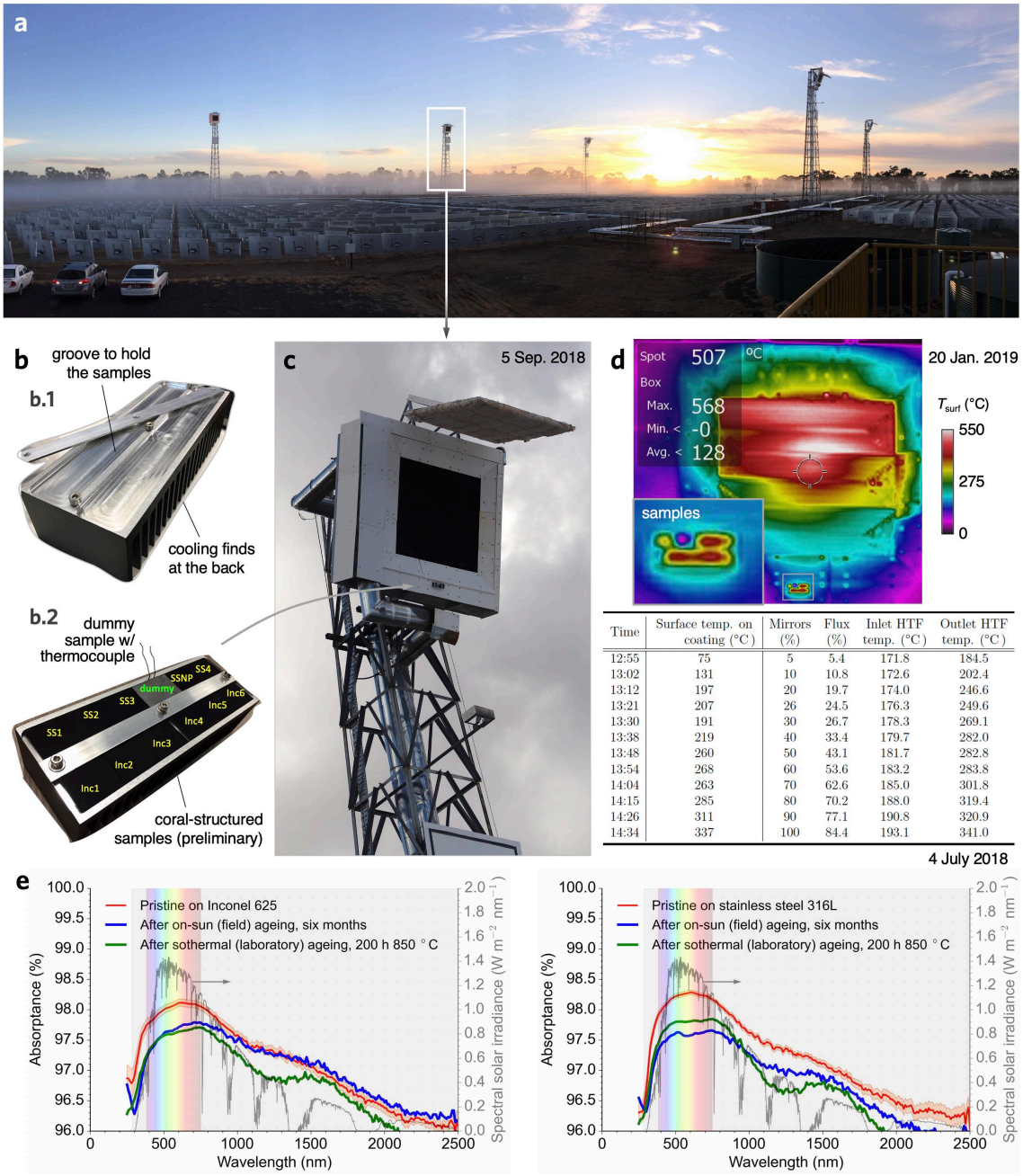

Time	Surface temp. on coating (°C)	Mirrors (%)	Flux (%)	Inlet HTF temp. (°C)	Outlet HTF temp. (°C)
12:55	75	5	5.4	171.8	184.5
13:02	131	10	10.8	172.6	202.4
13:12	197	20	19.7	174.0	246.6
13:21	207	26	24.5	176.3	249.6
13:30	191	30	26.7	178.3	269.1
13:38	219	40	33.4	179.7	282.0
13:48	260	50	43.1	181.7	282.8
13:54	268	60	53.6	183.2	283.8
14:04	263	70	62.6	185.0	301.8
14:15	285	80	70.2	188.0	319.4
14:26	311	90	77.1	190.8	320.9
14:34	337	100	84.4	193.1	341.0

Fig. S18 | High-flux, high-temperature durability test in a realistic CST environment. a, The concentrating solar thermal (CST) power plant in Australia (© Vast Solar) where the on-sun test was conducted on laboratory-made samples. **b**, A sample stand consisting of a metallic base with grooves to fit the samples and cooling fins extending from the back (**b.1**); eleven samples (*preliminary*) were fixed together with a dummy sample clamping a thermocouple for a direct temperature measurement (**b.2**). **c**, The samples were fixed in the spillage region of a commercial receiver, i.e. the region where the concentrated flux is less than that imparted onto the receiver surface, just below the heated surface to avoid overheating due to convection. **d**, Temperature measurement with an infra-red camera (top) for both the receiver surface and the samples; the experiment was initiated in July 2018 and concluded in January 2019; the surface temperature of the samples, external surface of the receiver, and inlet/outlet temperature were also recorded intermittently (below; table). **e**, Spectral absorptance for pristine samples, a sample aged in the on-sun testing for six months, and a sample accelerated isothermally at 850°C for 200 h (inside the furnace), when coated on Inconel 625 (left) and stainless steel 316L (right). The similarity in the results after ageing for on-sun and isothermal furnace ageing supports the conjecture that realistic coating degradation can be simulated by introducing higher temperatures for shorter time periods.

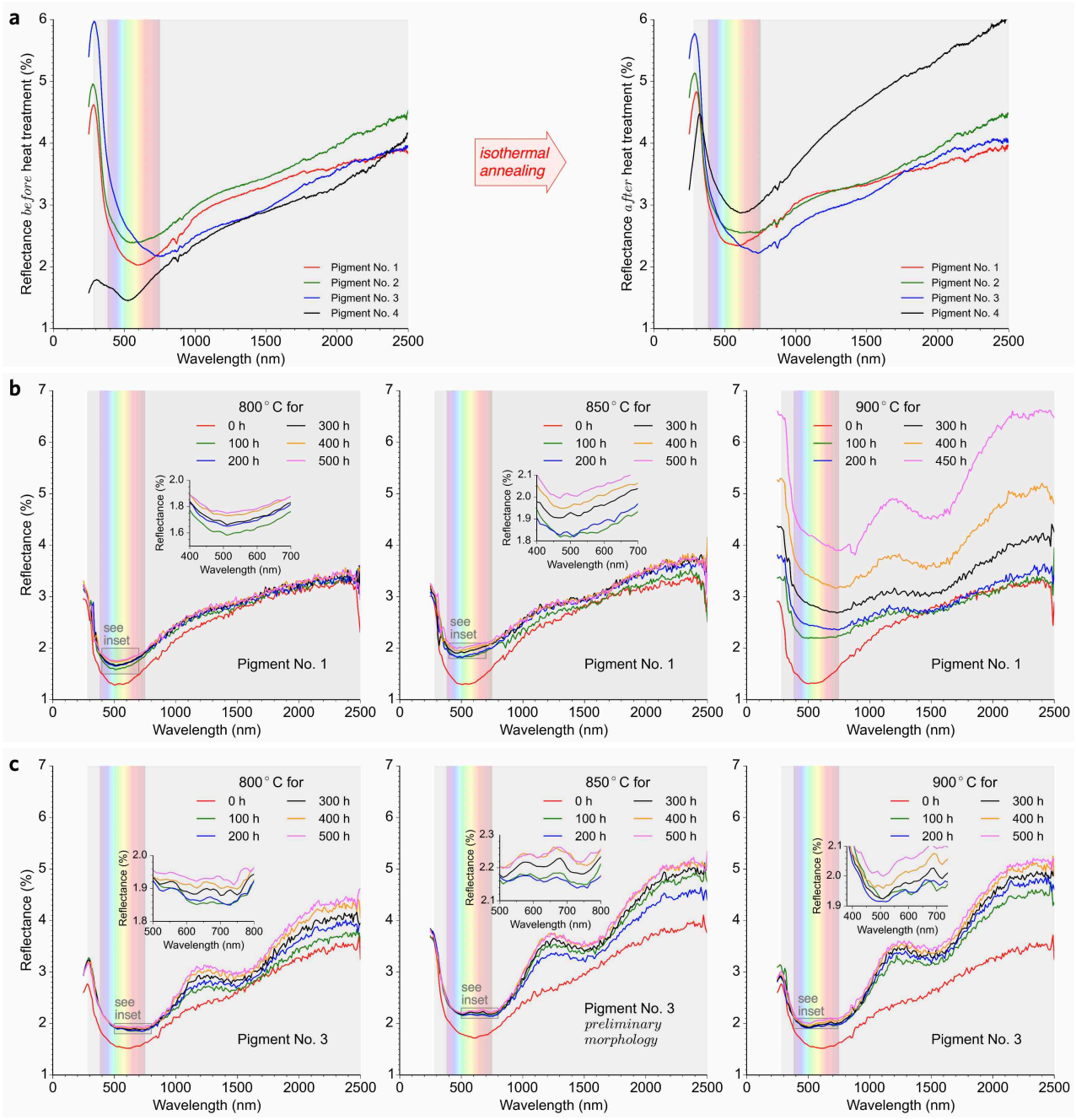

Fig. S19 | Spectral absorptance of promising spinels, before and after heat treatment. Coatings on stainless steel 316L. From a wide test of 18 different pigments, four were down selected for further testing based on their spectral absorptance. The supplier and estimated material composition is as follows. Pigment **No. 1**: $Cu_{0.73}Cr_{1.11}Mn_{1.16}O_4$ (42-303B, Tokan Material Technology Co., Ltd.), **No. 2**: $Cu_{0.47}Cr_{1.29}Mn_{1.24}O_4$ (Black 20C920, The Shepherd Color Company), **No. 3**: $Cu_{0.64}Cr_{1.51}Mn_{0.85}O_4$ (3250LM, Asahi Kasei Kogyo Co., Ltd.), and **No. 4**: $Cu_{1.09}Fe_{0.5}Mn_{1.41}O_4$ (F-6331-2, Ferro Corporation), which is essentially the same composition as the spinel pigments in the coating reported in Ref. [7]. **a**, Spectral reflectance for the *preliminary* coral-structured coating using the four selected pigments; in pristine condition (left), and after heat treatment for 2 h at 800°C (right). Pigments No.1 and 3 were identified as the most promising based on the low reflectance after short-term heat treatment. **b**, Spectral reflectance during long-term ageing for a coating with *improved* coral-structured morphology using pigments No. 1 after isothermal ageing at 800, 850, and 900°C (from left).The length scale of damaged features is confirmed with SEM analysis in **Fig. S20c**. **c**, Same as panel **b** but for pigment No. 3; however, the sample aged at 850°C has the *preliminary* morphology, whereas the samples aged at 800 and 900°C have *improved* macro-scale morphologies. Excellent stability was obtained for pigment No. 3 at 900°C.

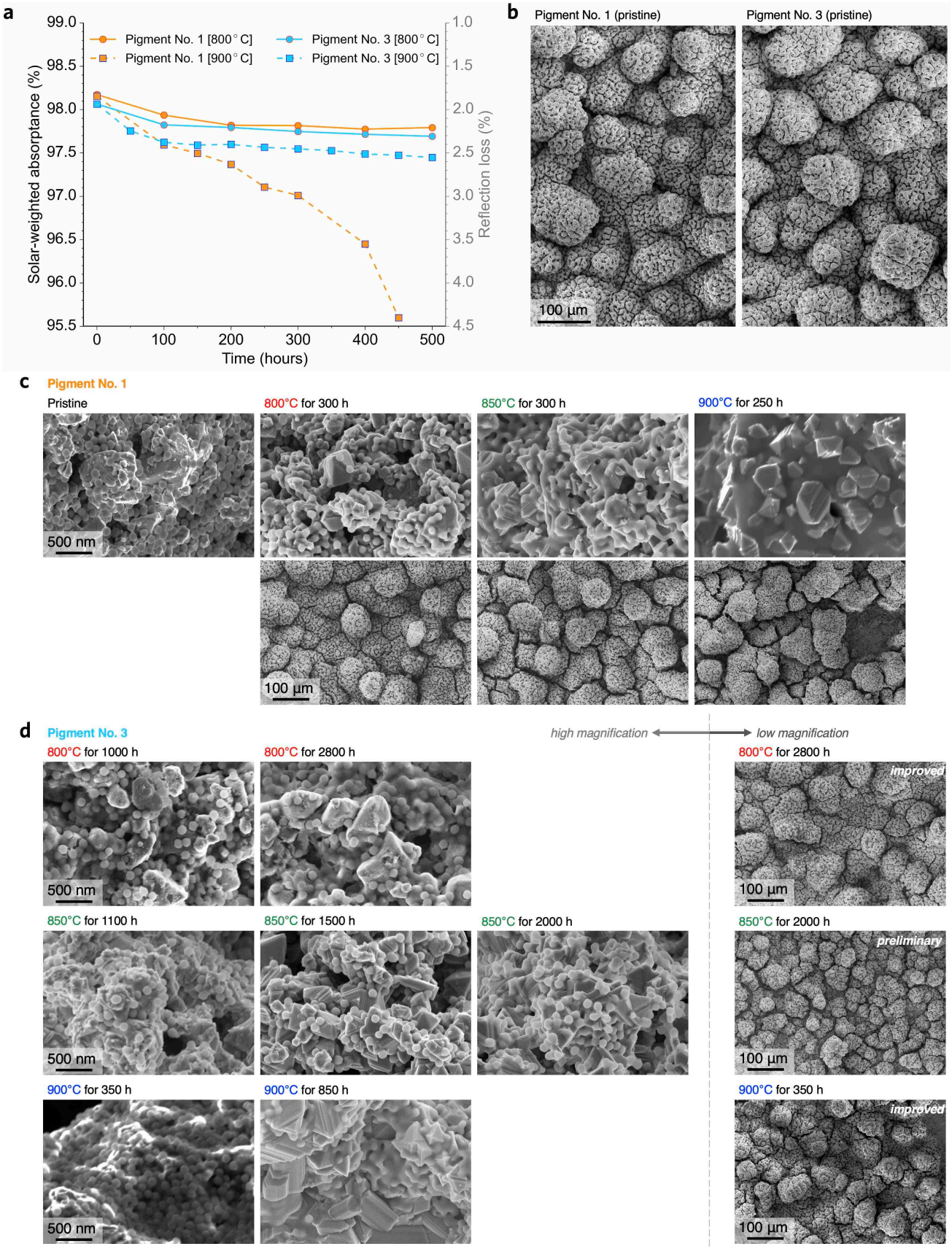

Fig. S20 | Solar-weighted absorptance and SEM analysis for the two most promising pigments. **a**, Solar-weighted absorptance of long-term aged samples at 800 and 900°C for the *improved* coating macro-scale morphology using pigment No. 1 (orange) and pigment No. 3 (light blue). In pristine condition, pigments No. 1

and No. 3 had a solar-weighted absorptance of 98.17% and 98.06%, respectively. The superior durability of pigment No. 3 ($Cu_{0.64}Cr_{1.51}Mn_{0.85}O_4$) when aged at 900°C resulted in its selection for the coatings presented in the article. **b**, The same macro-scale morphology (*improved*) was obtained when using both pigments. **c**, The coating using pigment No. 1: high and low magnification SEM images (top and bottom, respectively) when aged at three temperatures: 800, 850, and 900°C. Sintering of silica nanospheres was confirmed for 850 and 900°C after 300 and 250 h, respectively. Strong cracking was also observed, with peeling off starting at 900°C after 250 h. **d**, The coating using pigment No. 3: high and low magnification SEM images. Although crystallisation of pigments was observed, sintering of the silica nanospheres was mild even after ageing times longer than those reported for pigment No. 1 in panel **c**. Cracking and peeling off regions are less severe than for pigment No. 1. The test results show that pigment No. 3 has a better adhesion to the titania binder in the absorption layer and better compatibility (less reactive) with the silica matrix/nanospheres in the top layer.

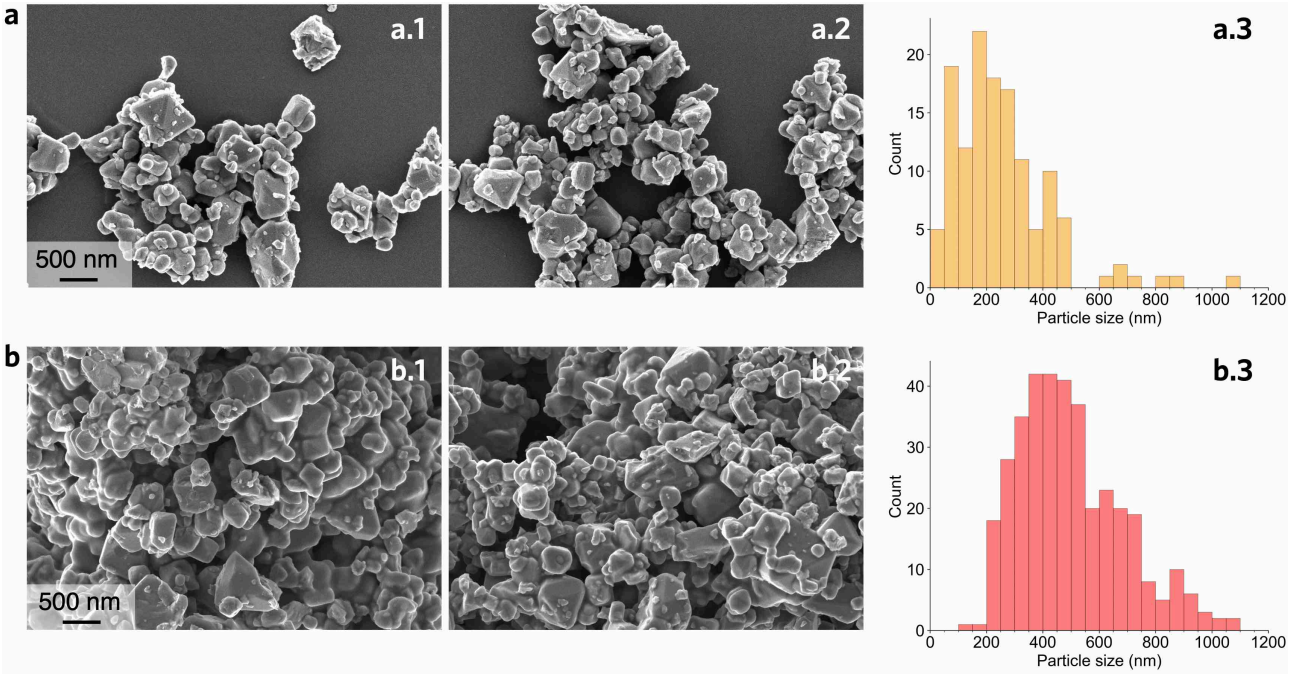

Fig. S21 | Pigment size distribution before and after absorption layer deposition. a, Pigment No. 3 as delivered, analysed from SEM images (representative images in panels **a.1** and **a.2**) to determine the particle size distribution (panel **a.3**). **b**, Analysis from surface morphology of coral-structured coating without top layer; representative SEM images (panels **b.1** and **b.2**) and particle size distribution (panel **b.3**). The small particles were largely covered by the titania binder, shifting the mean particle size from 260 nm to 510 nm after depositing the coral-structured absorption layer. The manufacturer (Asahi Kasei Kogyo Co., Ltd.) reported a particle size of 700 nm measured with a Laser Scattering Particle Size Distribution Analyzer (Partica LA-960, HORIBA).

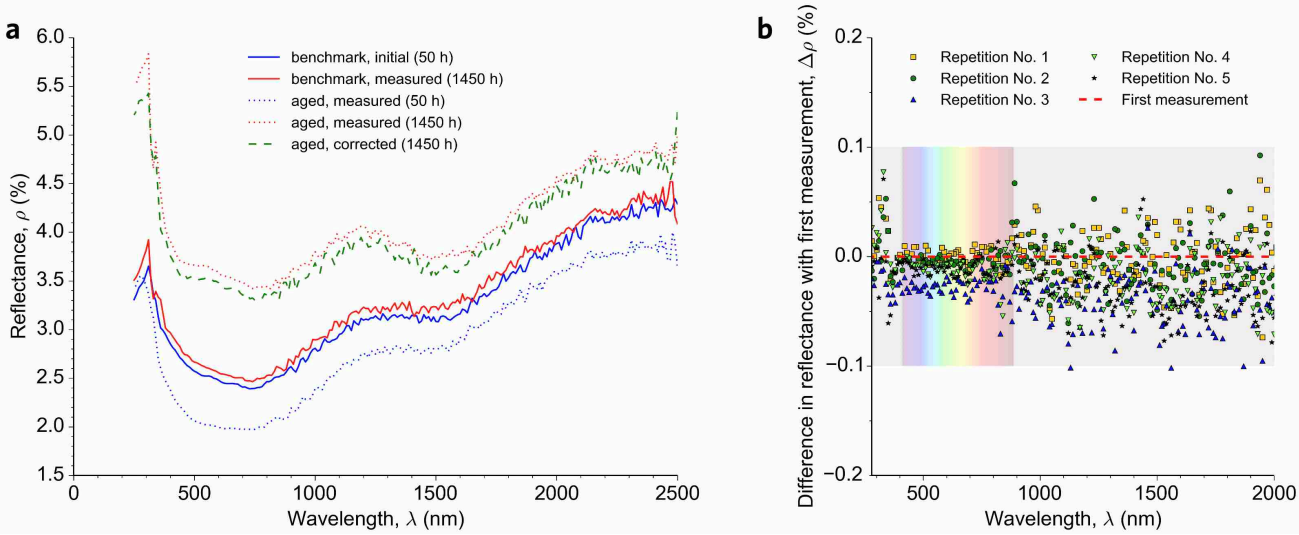

Fig. S22 | Correction of spectral reflectance measurements in long-term ageing tests. a, A correction is needed when making a relative comparison between two spectral measurements of directional-hemispherical reflectance taken at times far apart: e.g. 50 h and 1450 h (dotted blue and red curves) of a coral-structured coating on Inconel 625 aged at 900°C. A benchmark sample, which is not heat treated between measurements, may exhibit a slightly different value after instrument calibration (solid lines). The shift in value is consistent with the instrument accuracy. Therefore, in order to assess the relative change in spectral reflectance of the sample aged for 50 h and 1450 h (this is an example; generally, the initial sample is pristine), a correction of the measured reflectance was implemented (dashed green) based on the benchmark samples, following Eq. (4) in the Methods. **b**, The repeatability (precision) of the measurements was excellent, i.e. well within ±0.05% and ±0.1% in visible and near infrared ranges, respectively. Here, for each repetition, the sample was taken out of the spectrophotometer, rotated, and set back in (tangent to the integrating sphere).

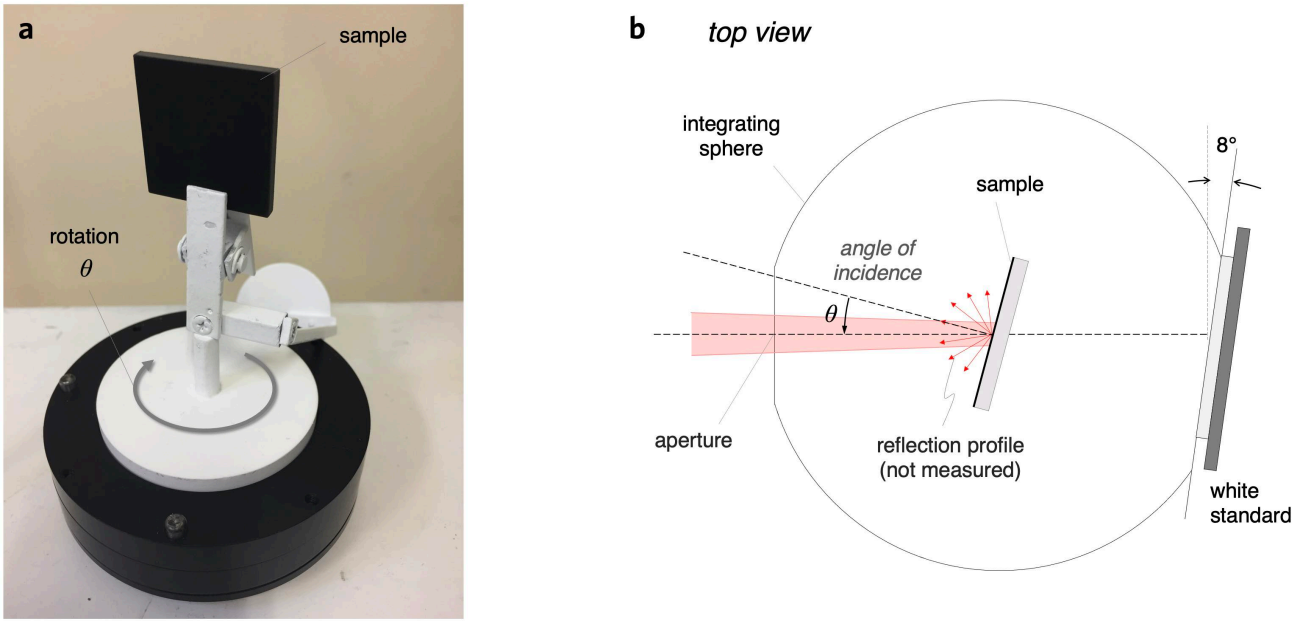

Fig. S23 | Setup for the measurement of the spectral directional-hemispherical reflectance. **a**, Add-on for the angular measurement with the spectrophotometer. The angle of incidence θ is set by rotating the stand. **b**, Top view schematic of the sample placed inside the integrating sphere, which is sealed with the white standard. The reported absorptance values for near-normal incidence have an angle of incidence of 8°.

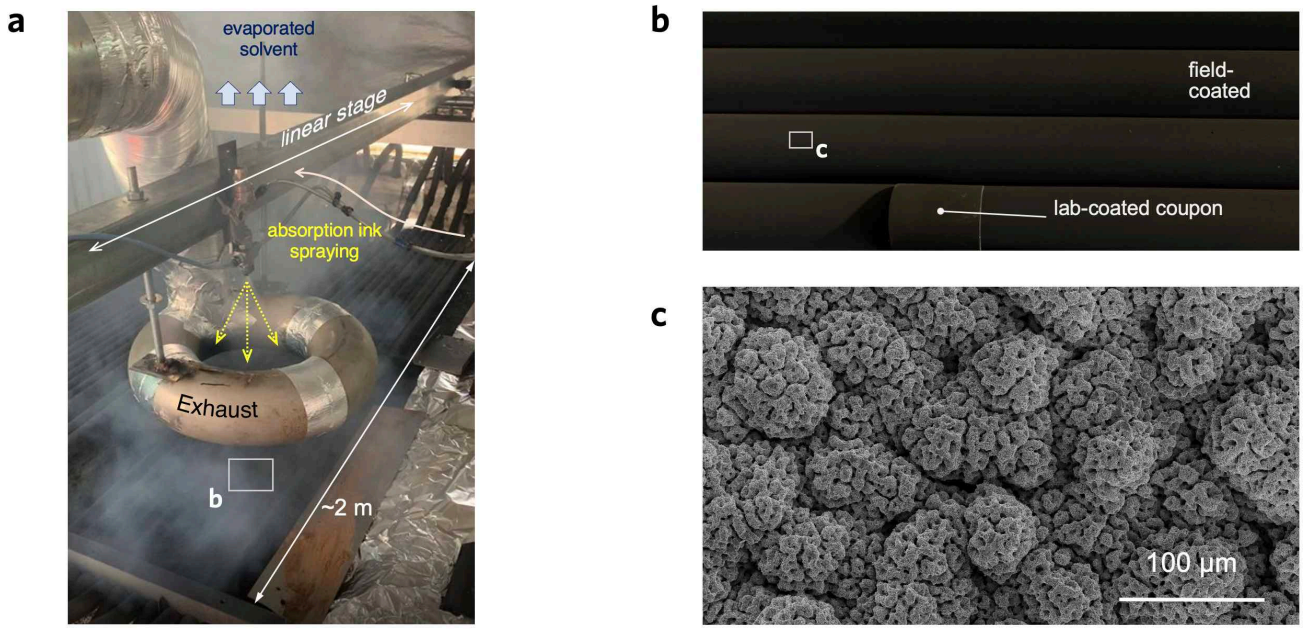

Fig. S24 | Scalability test on commercial receiver. **a**, Scalability experiment during the deposition of the absorption layer; the absorption solution has a large volume fraction of solvent, and thus the substrate needs to be kept at a suitable temperature for pyrolysis of Ti or Al coordinated compounds to occur. The doughnut-shaped exhaust helps remove the excess of evaporated solvent, which is necessary to create the multi-scale porosity, while circulation of heated oil through the receiver tubes helps guarantee that the surface temperature is kept nearly constant. **b**, Coated tubes overlaid with a lab-coated curved coupon. **c**, SEM image of the coral-structured coating on the coated tubes, showing an identical morphology as the lab-coated samples.

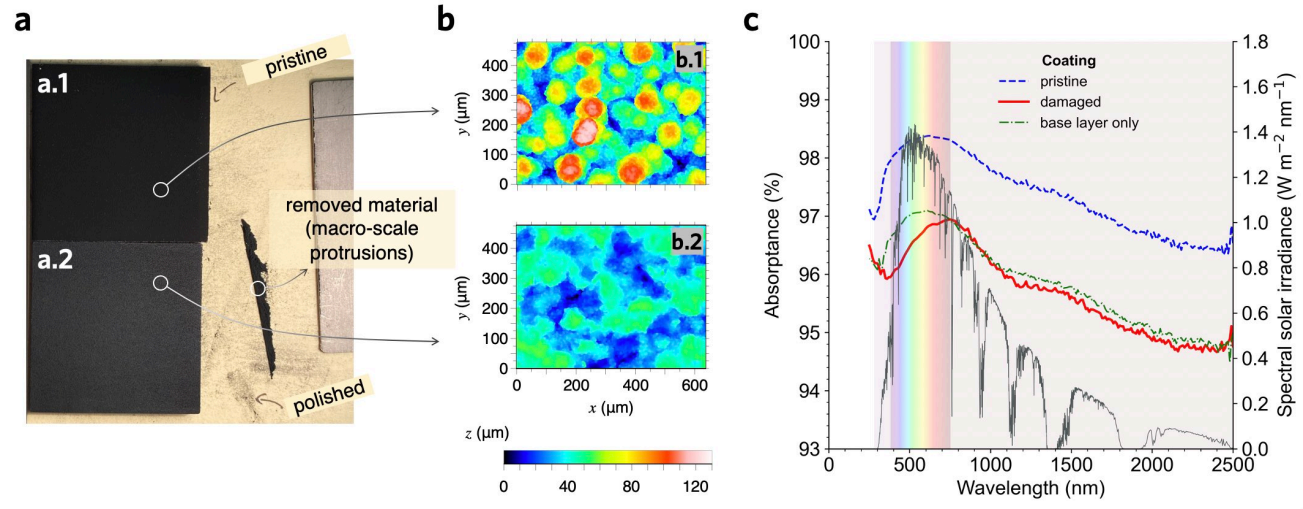

Fig. S25 | Testing of damaged coating with removed nano- and macro-scale features. **a**, Photo of a pristine (**a.1**) and damaged or 'polished' (**a.2**) coral-structured coating. The damaged coating has its nano- and macro-scale features peeled off, i.e. removed protrusions and top layer with nanospheres. **b**, Corresponding topography measurements with confocal microscopy. **b**, Corresponding spectral absorptance. The case of the base-layer only is also included for comparison with the damaged coating, which has a slightly lower spectral absorptance than in the visible range than the former.

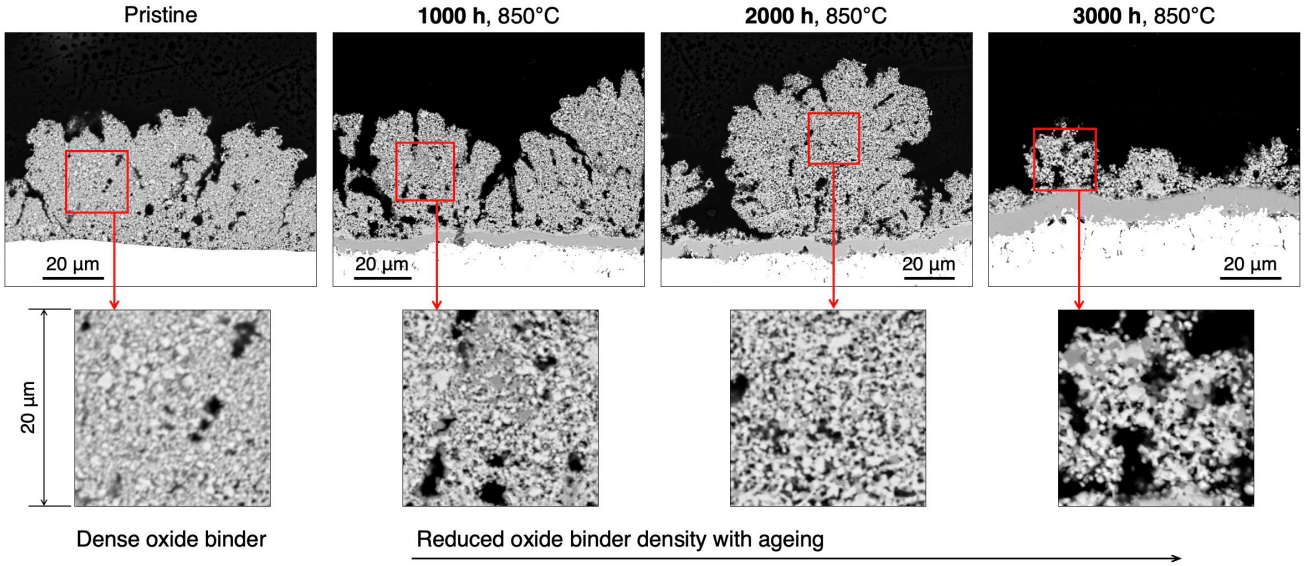

Fig. S26 | Cross-section SEM showing reduced oxide binder density with ageing. Our results indicate that the oxide binder is depleted as the ageing at 850°C progressed, as evidenced by an increase of voids (dark spots on the high-magnification cross-section SEM). The top SEM images show the cross-section morphology of the coral-structured coating on Inconel 625 in pristine condition and after ageing up to 3000 h. The bottom SEM images show a higher magnification region of 20 µm × 20 µm for each case whereby voids between the pigments (small black spots) become more prominent as the ageing progresses. In conjunction with the oxide layer growth, this increase of nano-porosity is thought to have contributed to mechanically weakening the coating, resulting in loss of material, as shown in the SEM image at 3000 h (right).

Supplementary Note 1: Black spinels for durable light absorbers

Spinels are a tightly packed crystal minerals that form in high temperature processes, thereby they help prevent the diffusion of oxygen or metal ions such as chromium, which makes spinel pigments highly stable at high temperatures. In CST applications, spinel pigments are usually held together by a porous binder and have reached absorptance of >97%,[8–11] but the coating still degrades rather rapidly during operation. The observed optical degradation is due to sintering of the nano-scale morphology, crystallisation of the binder, and cracking,[3] while the mechanical degradation is due to oxide layer growth since the nano-scale porosity is not effective in hindering diffusion of ions.[7] Therefore, research in CST coatings has evolved to improve durability while keeping the absorptance as close as possible to the pristine value. An absorptance of 99% by using nano-needle spinels has been reported,[10] but such a coating is expected to be weak against oxide layer growth from the substrate,[7] as well as due to sintering promoted by thermal cycling.[3]

In addition to the thermal stability under atmospheric conditions of the spinel pigments themselves, the long-term thermal stability of the coatings using a given spinel pigment is essential since a positive or negative interaction between the spinel pigments and other materials in the coating may occur, e.g. between the spinel pigments and the oxide binder, the top layer material, and/or the substrate (see discussion related to Fig. 1 in Ref. [7]). For example, despite the stability of both pigments No. 1 and No. 3 in air at elevated temperatures, the coating comprised of pigment No. 3 was found to be more stable than that comprised of pigment No. 1 after 450 h of ageing at 900°C (see characterisation in **Fig. S20**), possibly due to pigment No. 3 having more chromium content that could promote the growth of the protective chromium oxide layer at the coating–substrate interface (as reported in **Fig. S7**). Furthermore, the disappearance of silica nanospheres on the top layer and increased grain size around the pigments suggest that a negative interaction between pigment No. 1 and the top layer occurred. Likewise, as shown in **Fig. S19a**, the iron-based pigment No. 1 is less durable than the chromium-based pigments No. 2–3, possibly due to lack of chromium that promoted the growth of the protective chromium oxide layer at the coating-substrate interface (like that observed **Fig. S7**). This could justify why the coatings that are comprised of iron-based spinel pigments in Ref. [7] are less durable than the coatings comprised of chromium-based spinel pigments in Ref. [9] when deposited on nickel-based alloys.

Supplementary Note 2: Other potential benefits of coral morphology

The commercial benefits of a maintenance-free coating that can withstand the lifetime of the CST plant are significant. Currently in CST, re-coating large receivers after several years of use is the standard approach, which is a very costly process because the plant needs to shut down several days, and coating receivers in-situ 200 m above ground has proven to be an engineering challenge. Furthermore, in many CST applications, coated surfaces are exposed to shear force exerted by the natural convection boundary layer and airflow in the atmospheric boundary layer. The macro-scale roughness in the proposed coral-structured coating has the potential of reducing drag[12,13] and convective heat loss[14] due to vortices that form within the coral structure. The roughness can promote self-cleaning of dust particles,[15] which is also known to occur in coral structures.[16,17] These additional benefits can further improve the photothermal energy conversion in long-term CST applications. More details are given below.

Reduction in costs. The materials used to produce our coatings can be purchased in large quantities at comparable costs to those of conventional CSP coatings, such as Pyromark. We tested more than 18 different commercial spinel pigments, identifying the four best performing materials (**Fig. S19**; see suppliers in caption). To tune the micro- and macro- scale structures (**Fig. S14**), our coating needs large amounts of solvent, whereas large amounts of solvent are not required for Pyromark. However, these solvents are industrially produced in large quantities in the chemical industry and can be collected and reused. Furthermore, costs associated with the heating of the receiver surface while depositing the different layers (**Fig. S24**) are similar to those for curing Pyromark, which is a process that requires heating. Note that curing is not needed for our coating, balancing out costs. Importantly, our coating does not need grit blasting of the large receiver tubular surface, which is a costly process needed for Pyromark (albeit both our coating and Pyromark need chemical cleaning to remove oils).

Reduction in drag. The drag (shear force) exerted by the surrounding airflow can be a contributor to coating degradation. Therefore, drag reduction could be beneficial for the lifetime of the coating. A rough surface on the receiver can promote flow recirculation (i.e. small vortices between protrusions) that has the potential of drag reduction. Drag reduction by rough surfaces occurs in nature in animals other than coral reefs, e.g. in shark skins and other large fish.[18] However, the proposed coral-structured coating is not expected to reduce the drag as much as in the case of shark skin (because the micro-scale morphology is not aligned with the flow). Drag reduction due to such a multiscale fractal (or

hierarchical) surfaces including the tubular morphology (see **Fig. 2a**) is an interesting research area that has been addressed mainly from the point of view of geophysical flows.[19]

Reduction in thermal loss. We have shown that the macro-scale morphology can reduce both convective and radiative heat losses[14] because they create hot recirculating pockets of air and reduce the view factors, respectively.

Reduction in soiling. The shape of SiO_2 nanospheres could be further modified without changing their size to introduce superhydrophobic properties,[20] which could aid in soiling prevention.

Supplementary Note 3: Cross-section EDS elemental mapping

Cross-section elemental mapping of the coating on an Inconel 625 substrate in pristine condition and after ageing up to 3000 h at 800°C and 850°C are presented in **Figs. 4**, **N1** and **N2**. The results show that the oxide layer that formed between the coating and the substrate is uniform and compact with a thickness of < 9 μm. The oxide layer mainly consists of Cr and O with low concentration of Mn. **Figure N1c** demonstrates that the thickness of the oxide layer on the Inconel 625 substrate increases monotonically with increasing ageing temperature and duration for the analysed ranges. We found that increasing the ageing temperature from 800°C to 850°C increased the oxide layer growth rate threefold, from 0.50 nm h^{-1} to 1.43 nm h^{-1} (rate between 1000 h and 3000 h). The fact that Pyromark 2500 delaminated sooner than our coating (e.g. see ageing at 900°C in **Fig. 3e**), suggests that the oxide layer growth was larger, possibly due to its more prominent nano-porosity. It should be also noted that Al in the base layer diffused into the Inconel substrate after ageing at high temperatures which is in line with observations by Nofz et al.[21]

In addition, cross-section elemental mapping of the coating on a stainless steel 316L substrate in pristine condition and after ageing up to 3000 h at 800 and 850°C are presented in **Figs. N3**, **N4**. The results exhibit a compact oxide layer that formed after ageing at high temperatures which mainly contained Cr, O, and Mn (with no trace of Fe). The thickness of the oxide layer over the ageing period and at different temperatures are not compared due to the peeling off phenomenon that occurred during the cutting and fixing of the samples in epoxy resin. In contrast to the Inconel substrate, the aluminium diffusion from the coating into the stainless steel 316L substrate did not occur. However, we found that silicon diffused into the substrate under the oxide layer.

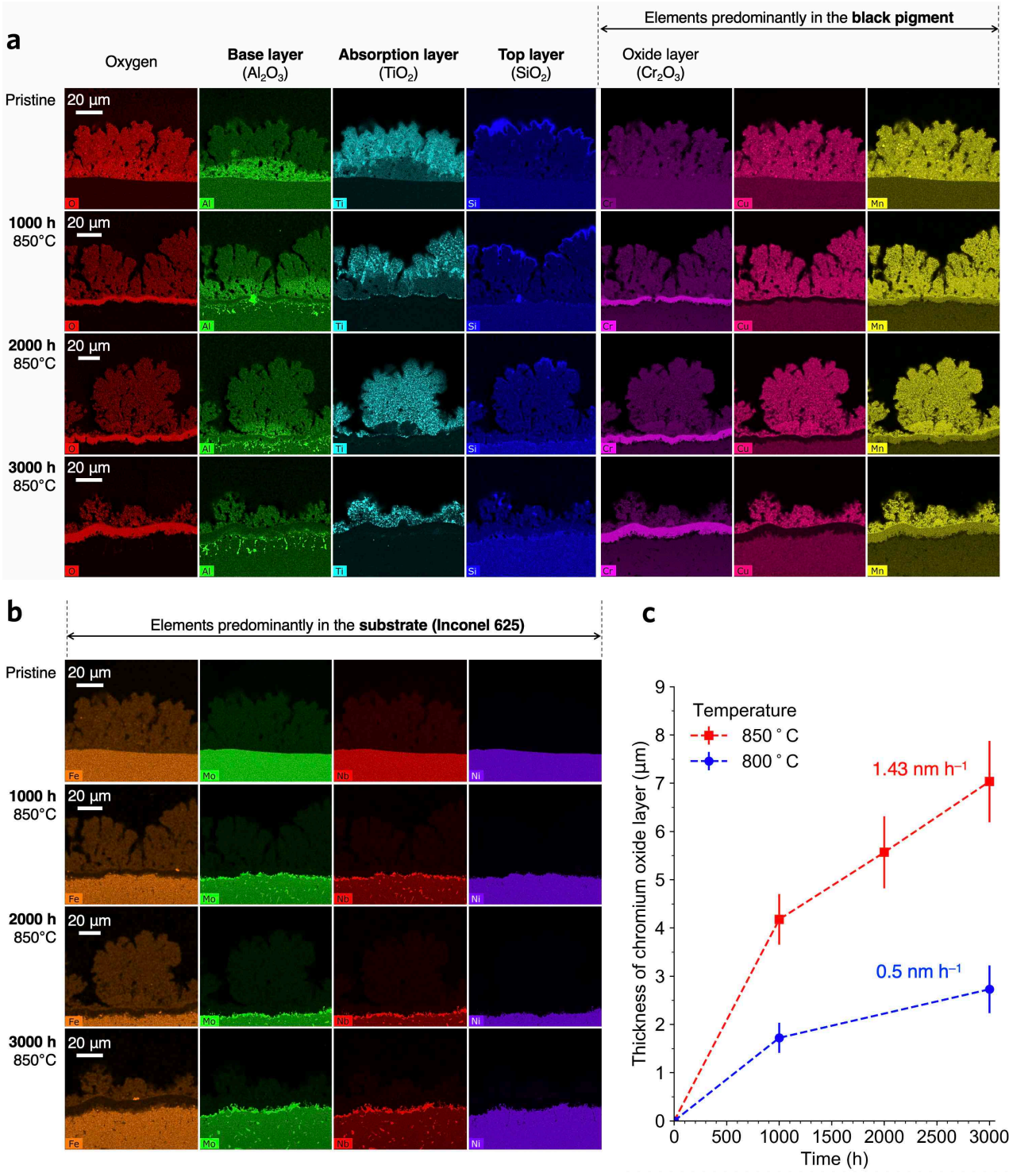

Fig. N1 | High-magnification elemental mapping of our coating on Inconel 625 aged at 850°C. Cross-section elemental mapping with high magnification for the proposed coating, in pristine condition and after ageing up to 3000 h. **a**, Oxygen together with elements predominantly in the base (alumina), absorption (titania) and top (silica) layers. **b**, Elements predominantly found in the substrate; note that Cr, Cu and Mn are found in both the black pigment and the substrate. **c**, The thickness of chromium oxide layer as a function of the isothermal ageing time (the results of ageing at 800°C are also included as a reference; see **Fig. 4b**). The marker and error bar indicate the average and ±standard deviation of the coating thickness, respectively, based on more than 20 measurements for each reported value. The less obvious coral morphology at 3000 h was due to damage that occurred when cutting the samples, as SEM images in **Fig. 4a** show a largely unchanged coral-structured morphology for uncut samples.

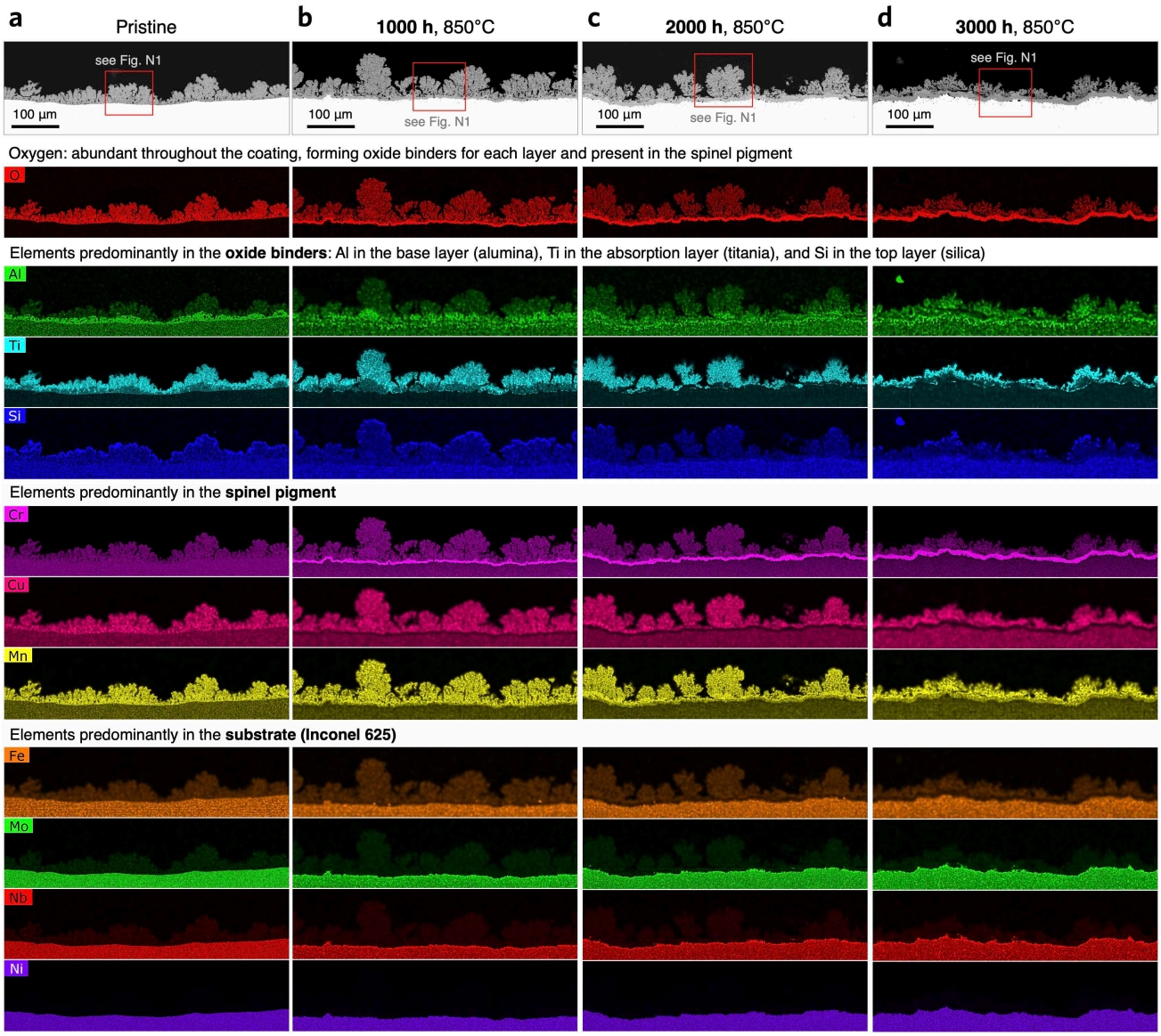

Fig. N2 | Low-magnification elemental mapping of our coating on Inconel 625 aged at 850°C. Cross-section analysis with low magnification with a back-scattered electron (BSE) image (top) and elemental mapping for the proposed coral-structured coating, in pristine condition (**a**) and after ageing for 1000 h (**b**), 2000 h (**c**) and 3000 h (**d**). The magnified regions shown in **Fig. N1** are indicated in the top BSE image. After oxygen, the elements are grouped for those predominantly in the oxide binder, spinel pigment and substrate. Cr, Cu and Mn are found in both the black spinel and the substrate.

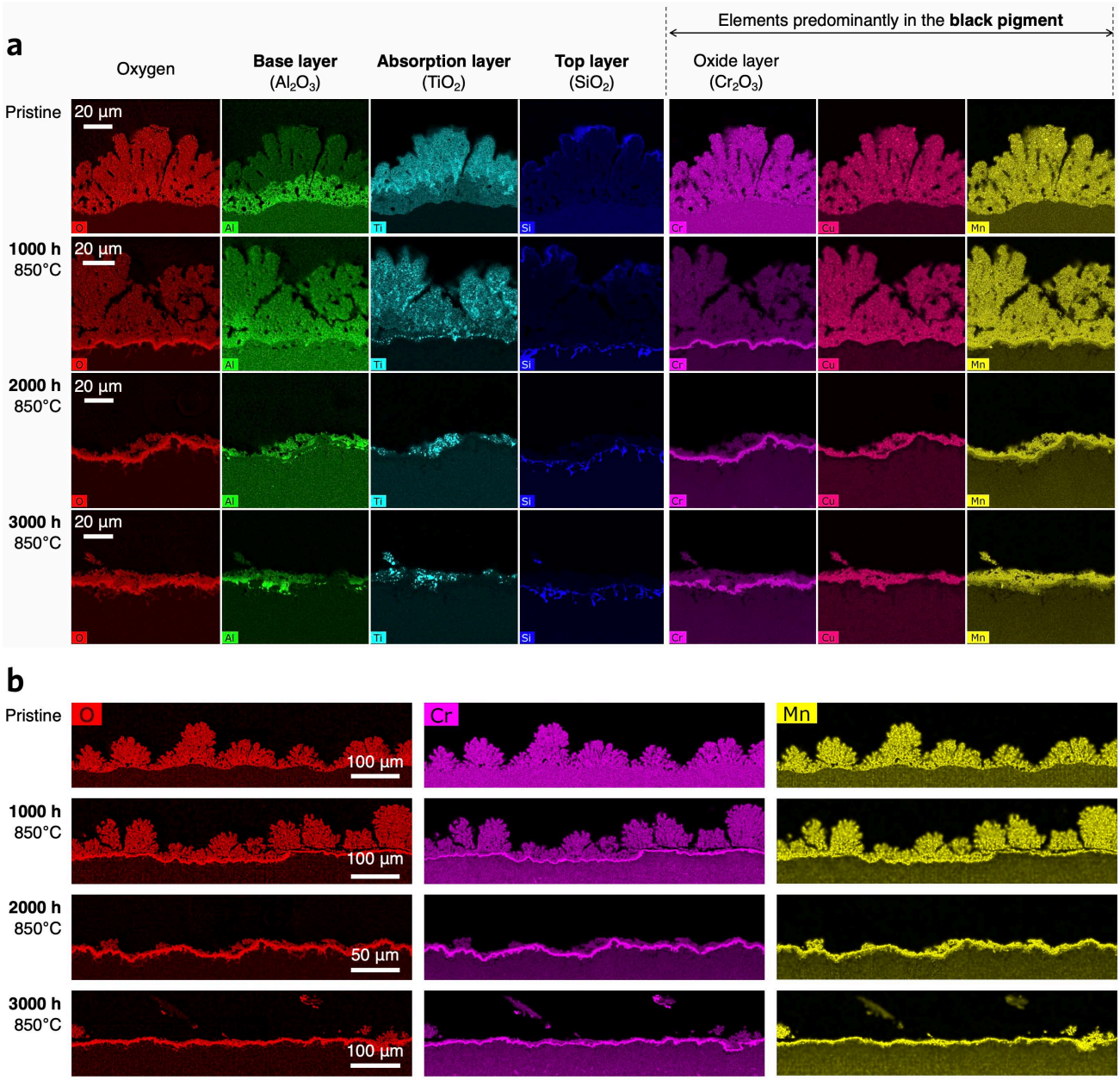

Fig. N3 | Elemental mapping of our coating on stainless steel 316L aged at 850°C. Cross-section elemental mapping with two magnifications. **a**, High-magnification images showing oxygen and those elements predominantly found in the base (alumina), absorption (titania), and top (silica) layers, as well as in the black pigments present throughout the coating. **b**, Low-magnification elemental mapping for O (left), Cr (middle) and Mn (right). The oxide layer growing between substrate and coating was difficult to analyse quantitatively for 2000 h and 3000 h because the coating peeled off during the processes of cutting and fixing in the epoxy resin for polishing.

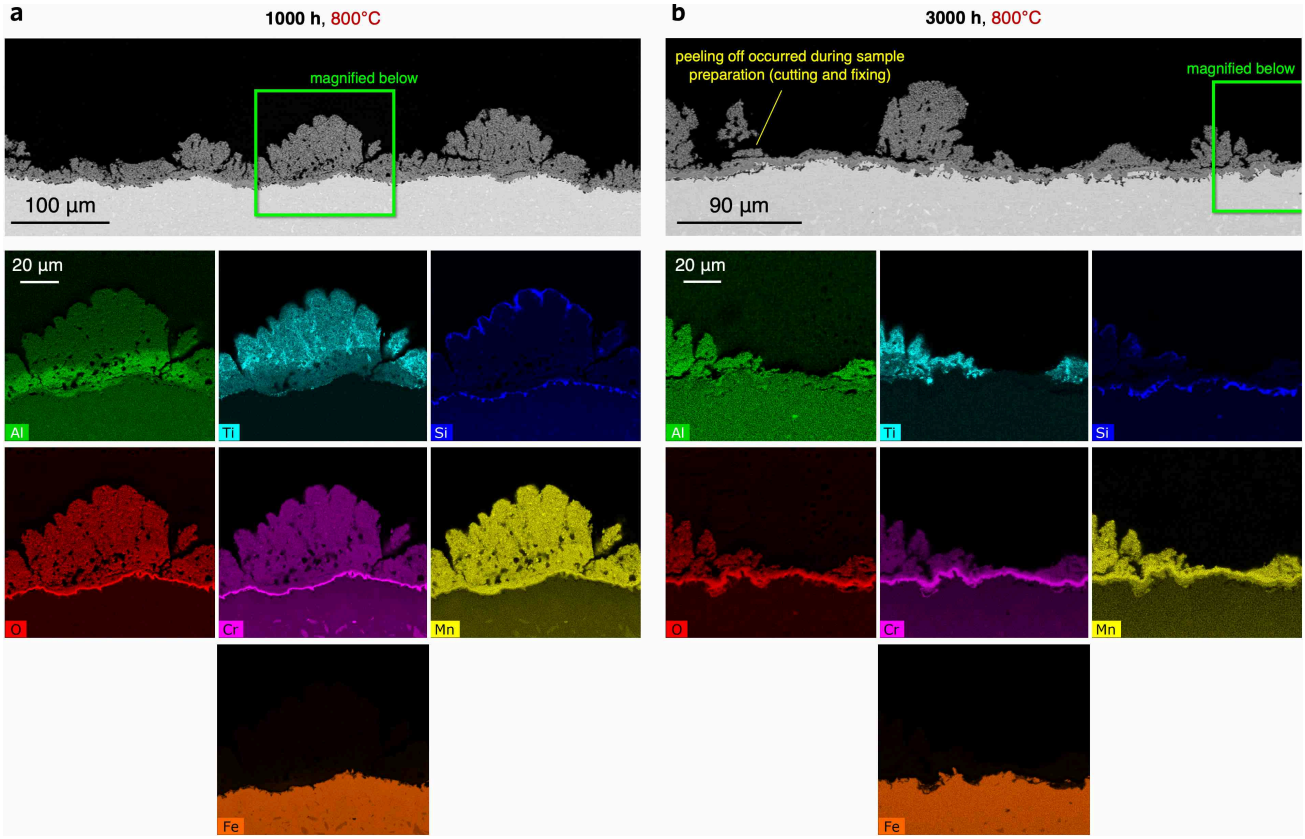

Fig. N4 | Elemental mapping of our coating on stainless steel 316L aged at 800°C. This figure shows the results for the proposed coral-structured coating on stainless steel 316L aged at 800°C, supplementary to **Fig. 4b** that corresponds to Inconel 625. **a**, At 1000 h, low-magnification BSE image (top) and slightly higher magnification elemental mapping, clockwise from top left: Al in the base layer, Ti in the absorption layer, Si in the top layer, O through the coating, Cr concentrated in the oxide layer, Mn in the black spinel pigments. **b**, At 3000 h, the same as panel (**a**). The peeling off occurred due to the sample preparation process, i.e. cutting and fixing in epoxy resin for polishing, as the top-view SEM images did not show such peeling off.

Supplementary Note 4: Short-term ageing on two kinds of substrate

Prior to the long-term ageing tests for thousands of hours, we conducted shorter-term (10 h, 100 h) isothermal ageing at three temperature values (600, 750, and 850°C) with the coatings on two kinds of substrate: stainless steels 316L (SS316L) and Inconel 625, for both the coral-structured coating (preliminary) and Pyromark 2500 coating (pre-optimisation). The spectral absorptance measurements are shown in **Figs. N5**–**N7**, while the solar-weighted absorptance is summarised in **Tables N1**, **N2** for the coatings on Inconel 625 and SS316L, respectively. The solar-weighted absorptance of the proposed coral-structured coating was significantly higher than that of the benchmark, maintaining an excellent absorptance and repeatability after ageing. The standard deviation for Pyromark was consistently higher mainly due to the impact of deliberate variation in coating thickness,[22] rather than repeatability effects.

The spectral absorptance of the pristine samples for the preliminary coral-structured coating on Inconel 625 (coating with three-layer, no primer) and stainless steel 316L (SS316L, coating with four layers including a primer) is shown in **Fig. N5**. The spectral absorptance of Pyromark, with coating thickness ranging from 5 to 35 μm, are included for comparison. The larger standard deviation for Pyromark in the pristine state is due to a larger thickness variation from 5 to 35 μm. The average solar-weighted absorptance for pristine Pyromark on Inconel 625 was α_{pyro} = 96.56% with a standard deviation of σ_{pyro} = 0.08%, and on SS316L was α_{pyro} = 96.72% with a standard deviation of σ_{pyro} = 0.12%. On the other hand, the average solar-weighted absorptance and standard deviation for the proposed coral-structured coatings on Inconel 625 were α_{coral} = 97.72% and σ_{coral} = 0.07%, and on SS316L were α_{coral} = 97.85% and σ_{coral} = 0.04%. The solid line in **Figs. N5**–**N7** indicates the mean value at each wavelength of the 36 samples on Inconel 625 and 35 samples on SS316L. The shaded region indicates the standard deviation $\pm\sigma$ from the mean value at each wavelength. In pristine state, the solar-weighted absorptance of coral-structured coatings is close to 98% (the improved morphology exceeded this value), ca. 1.2% increase from that of Pyromark. Note that comparison between coating absorptance values in this Note is given in relative percentage from that of Pyromark (see relative improvement in **Tables N1**, **N2**). Furthermore, the low standard deviation indicates that coral-structured coatings are highly reproducible.

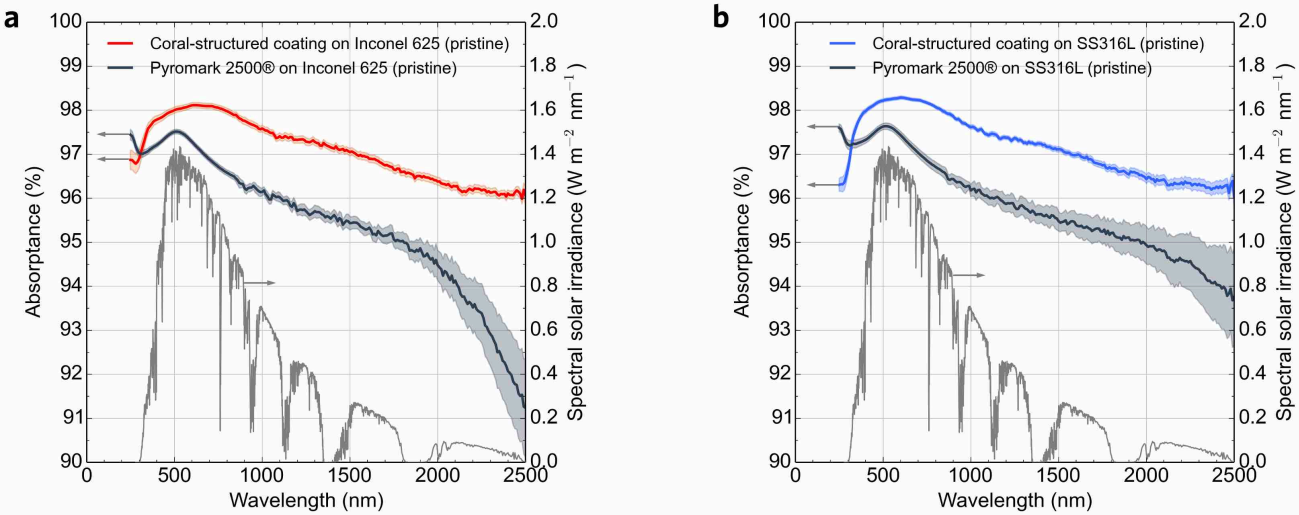

Fig. N5 | Spectral absorptance of coral-structured and Pyromark coatings in pristine condition. Absorptance (left axis) and solar irradiance (right axis) as a function of wavelength. The coral-structured coating has the preliminary morphology, while the Pyromark coating is pre-optimisation. **a**, Coatings on Inconel 625. **b**, Coatings on stainless steel 316L (SS316L). The coral-structured coating performs better over the entire wavelength spectrum, except in the violet/ultraviolet range where the solar irradiance is weak.

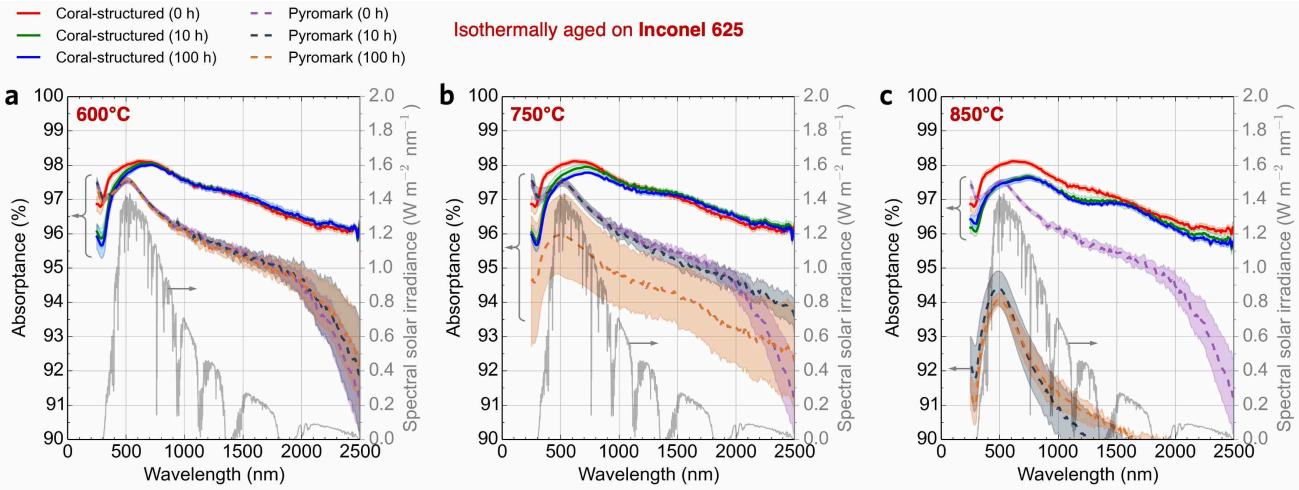

Fig. N6 | Spectral absorptance of coatings on Inconel 625 after ageing up to 100 h. Absorptance (left axis) as a function of wavelength for coatings on *Inconel 625* after ageing isothermally at three temperatures for 10 h and 100 h. The same legend applies to all plots. The coral-structured coating has the preliminary morphology, while the Pyromark coating is pre-optimisation. **a**, After ageing at 600°C. **b**, After ageing at 750°C. **c**, After ageing at 850°C.

Table N1 | Solar-weighted absorptance after ageing at 600, 750, 850°C for 10, 100 h on Inconel 625. The solar-weighted (SW) absorptance of the preliminary coral-structured coating for short ageing periods of 10 h and 100 h, at three isothermal ageing temperatures of 600, 750, and 850°C on a substrate of *Inconel 625*. Values corresponding to the coral-structured coating (blue), Pyromark 2500 (red), and the relative improvement (green) are listed. The relative improvement is calculated as $(\alpha_{coral} - \alpha_{pyro})/\alpha_{pyro} \times 100$, where α_{coral} is the α_{SW} of the coral-structured coating and α_{pyro} is that for Pyromark; a positive relative improvement indicates an increase in α_{SW} for average, minimum and maximum values, whereas a negative value in the standard deviation indicates an improvement in reproducibility (reduction of variability). A correction of the spectral hemispherical reflectance using Eq. (4) was not necessary because the ageing time was rather short, and no calibration of the instrument was conducted in between measurements.

Coral-structured coating (blue) Pyromark 2500® coating (red)		Average value (%)	Standard deviation (%)	Minimum value (%)	Maximum value (%)	No. of samples
	Pristine	97.72	0.07	97.59	97.85	36
		96.56	0.08	96.44	96.74	14
	relative improvement	+1.20	–11.97	+1.19	+1.15	
600°C	10 h	97.66	0.05	97.58	97.71	5
		96.56	0.07	96.52	96.66	3
	relative improvement	+1.14	–21.53	+1.10	+1.09	
	100 h	97.59	0.06	97.51	97.67	5
		96.52	0.06	96.49	96.62	3
	relative improvement	+1.11	–8.30	+1.06	+1.09	
750°C	10 h	97.57	0.08	97.43	97.66	5
		96.57	0.14	96.35	96.68	4
	relative improvement	+1.04	–39.11	+1.13	+1.01	
	100 h	97.43	0.05	97.35	97.48	5
		95.35	0.86	94.03	95.96	4
	relative improvement	+2.18	–94.45	+3.53	+1.59	
850°C	10 h	97.31	0.08	97.22	97.41	5
		92.24	0.55	91.42	92.56	3
	relative improvement	+5.50	–86.14	+6.34	+5.24	
	100 h	97.30	0.08	97.20	97.39	6
		92.41	0.28	92.16	92.65	3
	relative improvement	+5.29	–70.28	+5.47	+5.12	

The spectral absorptance for the coated samples on Inconel 625 in pristine state and after ageing at 600, 750, and 850°C after 10 and 100 h are shown in **Fig. N6**. The results are compared with reported measurements of spectral absorptance for Pyromark on the same substrate.[22] The repeatability is assessed by the standard deviation for each batch of five or six samples and is indicated by the shaded

region in the plots. The average and standard deviation of the solar-weighted absorptance of coral-structured samples aged at 850°C on Inconel 625 were α_{coral} = 97.31% and σ_{coral} = 0.08% after 10 h (**Table N1**), while for six samples were α_{coral} = 97.30% and σ_{coral} = 0.08% after 100 h. The reduction in absorptance from pristine is only 0.42% even after 100 h of ageing, and the low standard deviation indicates that these coatings are highly reproducible. At 750°C for 100 h, the solar-weighted absorptance and standard deviation became α_{coral} = 97.43% and σ_{α} = 0.05%, whereas at 600°C for 100 h the results were α_{coral} = 97.59% and σ_{α} = 0.06%, i.e. a marginal decrease from the pristine value of 97.72%.

The spectral absorptance for the coated samples on SS316L in pristine state and after ageing at 600, 750, and 850°C after 10 and 100 h are shown in **Fig. N7**. The results are compared with reported measurements of spectral absorptance for Pyromark on the same substrate.[22] The repeatability is assessed by the standard deviation for each batch of five or six samples (shaded region in the figure). The coral-structured coating on SS316L aged at 850°C yielded an average solar-weighted absorptance and standard deviation of α_{coral} = 97.53% and σ_{coral} = 0.07% after 10 h (**Table N2**) and α_{coral} = 97.43% and σ_{coral} = 0.07% after 100 h. The reduction in absorptance from pristine (average of 35 samples) is only 0.42% after 100 h of ageing, which compares to a drop of 3.6% in Pyromark under the same ageing conditions. Once again, the low standard deviation, even after ageing, indicates the good repeatability. At 750°C after 100 h of ageing, the absorptance and standard deviation were α_{coral} = 97.68% and σ_{coral} = 0.06%, and at 600°C after 100 h, α_{coral} = 97.84% and σ_{coral} = 0.02%. At the lower temperature of 600°C, the absorptance value is very similar to the pristine value of 97.85%, and even increased slightly after 10 h (to α_{coral} = 97.87%), which suggests the change of phase in the material, possibly from amorphous TiO_2 to anatase TiO_2 (the rutile phase was identified for ageing temperatures greater or equal to 800°C).

SEM images showing the coating morphology in pristine condition and after ageing at 850°C for 10 h and 100 h are shown in **Fig. N8**. All the length scale morphologies are kept. For example, the same well-defined coral-structured macro-scale was observed before ageing (**Fig. N8a**) and after (**Fig. N8b**, **c**). No coating failure was observed after ageing. Likewise, no major cracks or failure were observed after ageing.

Table N2 | Solar-weighted absorptance after ageing at 600, 750, 850°C for 10, 100 h on SS316L. The same explanation as in the caption of **Table N1**, but using *stainless steel 316L* (SS316L) instead of Inconel 625 as substrate. The absolute values of solar-weighted absorptance for the coatings on SS316L are slightly larger than in the case of having the coatings on Inconel 625. The standard deviation is generally larger for Pyromark 2500 on SS316L than on Inconel 625, with values as large as 0.89% (10 h at 850°C). In contrast, the standard deviation for the coral-structured coating did not exceed 0.08% on either SS316L or Inconel 625 (**Table N1**).

Coral-structured coating (blue) Pyromark 2500® coating (red)		Average value (%)	Standard deviation (%)	Minimum value (%)	Maximum value (%)	No. of samples
	Pristine	97.85	0.04	97.73	97.93	35
		96.72	0.13	96.34	96.84	14
	relative improvement	+1.17	–71.36	+1.45	+1.13	
600°C	10 h	97.87	0.02	97.85	97.89	5
		96.65	0.23	96.30	96.79	4
	relative improvement	+1.26	–93.09	+1.61	+1.13	
	100 h	97.84	0.02	97.81	97.87	5
		96.57	0.22	96.29	96.76	4
	relative improvement	+1.31	–89.07	+1.58	+1.15	
750°C	10 h	97.72	0.07	97.59	97.76	5
		96.50	0.15	96.31	96.66	4
	relative improvement	+1.26	–51.67	+1.33	+1.14	
	100 h	97.68	0.06	97.65	97.80	6
		94.42	0.55	93.86	95.15	4
	relative improvement	+3.46	–89.79	+4.03	+2.79	
850°C	10 h	97.53	0.07	97.45	97.62	5
		92.34	0.89	91.54	93.58	4
	relative improvement	+5.61	–92.56	+6.45	+4.31	
	100 h	97.43	0.07	97.35	97.51	5
		93.09	0.60	92.36	93.74	4
	relative improvement	+4.67	–88.70	+5.40	+4.03	

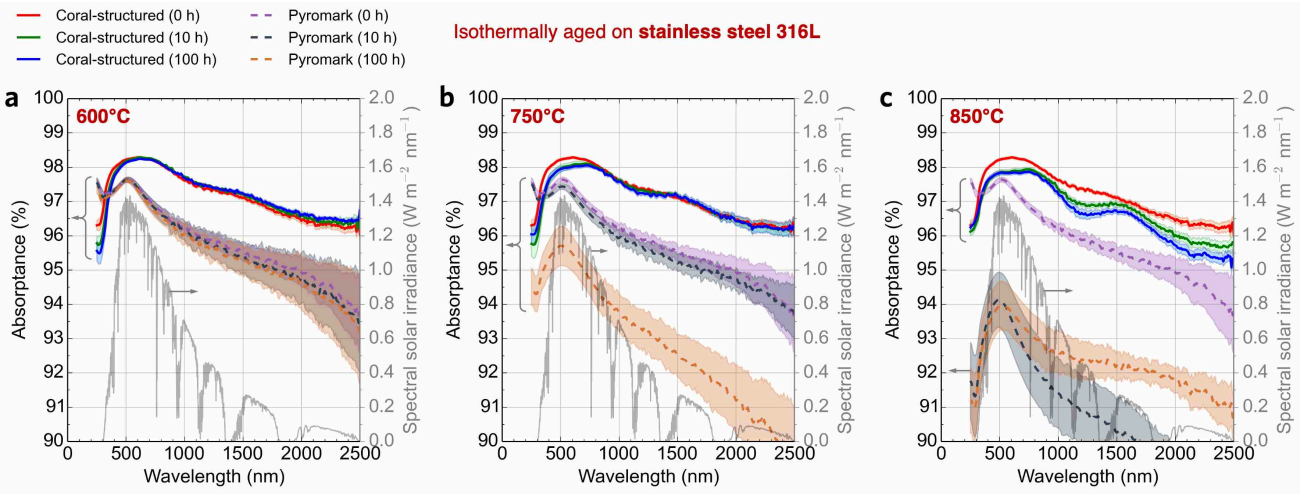

Fig. N7 | Spectral absorptance of coatings on SS316L after ageing up to 100 h. Absorptance (left axis) as a function of wavelength for coatings on the *stainless steel 316L* substrate after ageing isothermally at three temperatures for 10 h and 100 h. The same legend applies to all plots. The coral-structured coating has the preliminary morphology, while the Pyromark coating is pre-optimisation. **a**, After ageing at 600°C. **b**, After ageing at 750°C. **c**, After ageing at 850°C.

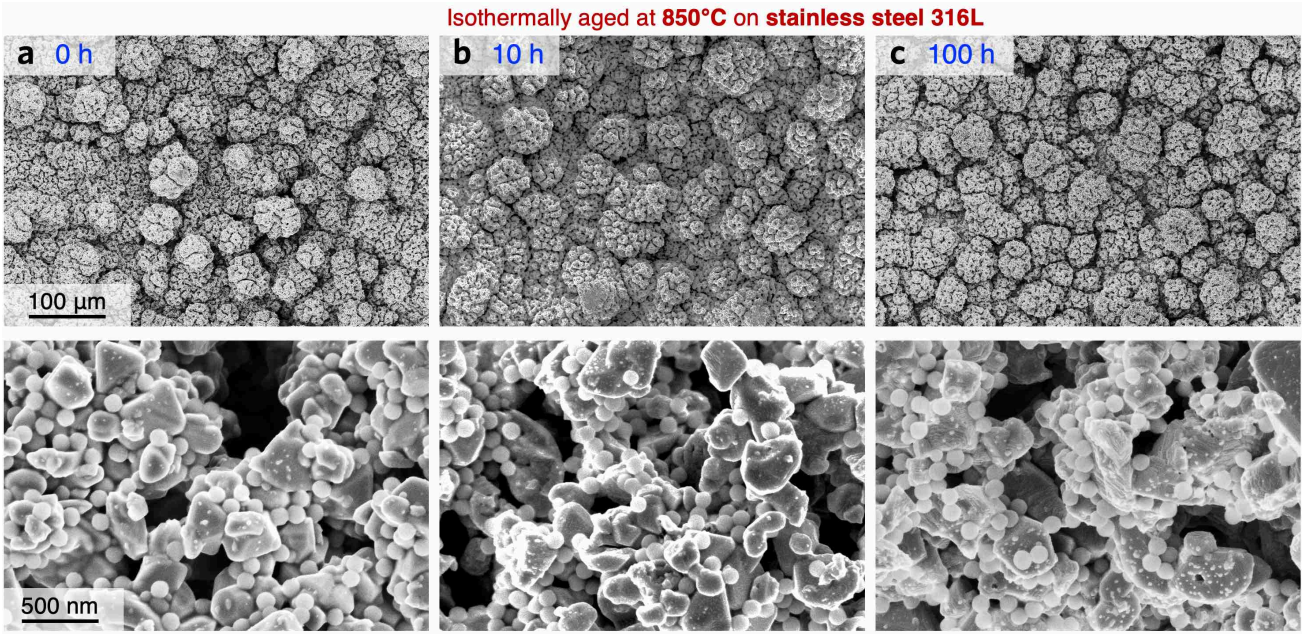

Fig. N8 | SEM images of coatings on SS316L: pristine and after ageing at 850°C, up to 100 h. Low magnification (top images) and high magnification (bottom images) SEM images of preliminary coral-structured coating in pristine condition (panel **a**), after ageing for 10 h (panel **b**) and 100 h (panel **c**) at 850°C. Both macro-scale coral-structured morphology (top) and nano-scale sphere and pigment morphology (bottom) are largely unchanged. The micro-scale morphology (open micropores; not shown) is situated between these two magnifications (see **Fig. 2a**).

Supplementary Note 5: Top layer solution preparation

To prepare the top solution, a tetraethyl orthosilicate mixture (mixture A) was added to a mixture with silica nanosphere reacted with a tetraethyl orthosilicate (mixture B) and then diluted with ethanol. The detailed process for producing both mixtures is explained in **Figs. N9**, **N10**.

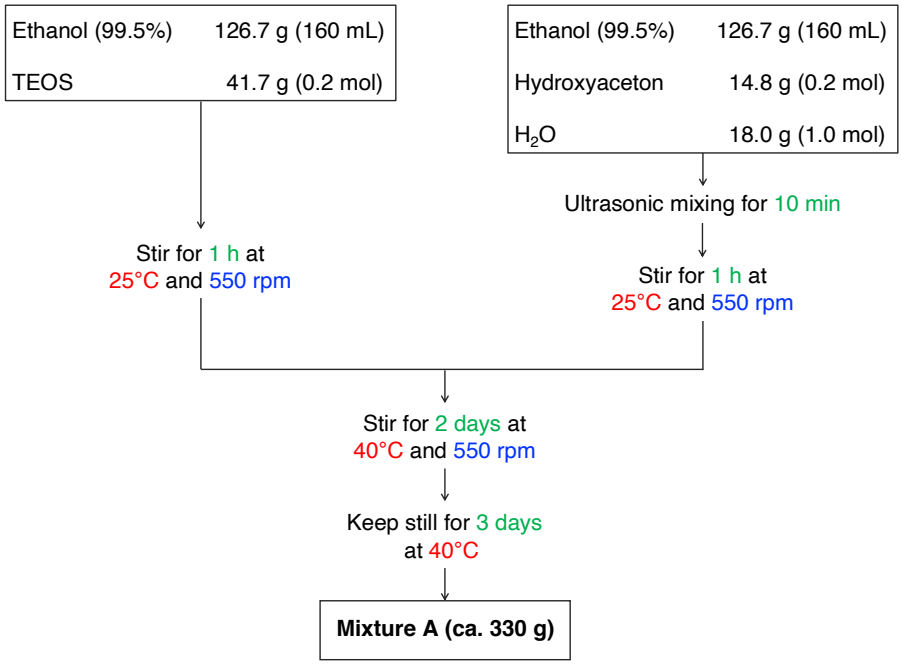

Fig. N9 | Preparation procedure of mixture A (top layer): porous silica coating solutions. This process yields ca. 330 g of mixture A, which is a porous silica matrix used in the top layer solution. The molecular mass for tetraethyl orthosilicate (TEOS) is 208 Da, while that for silica (SiO_2) is 60.1 Da. The composition of silica in the end-product was measured to be 4.0 wt%, which was close to the calculated value of 3.7 wt%. Mixture A is used with mixture B (explained in Methods) to produce the top layer solution.

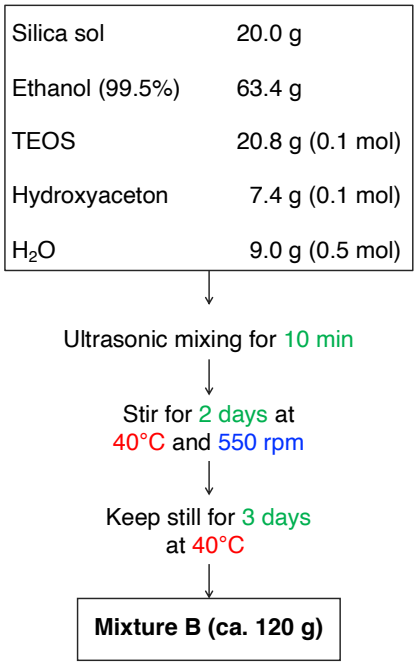

Fig. N10 | Preparation procedure of mixture B (top layer): silica nanosphere coating solution. This process yields ca. 120 g of mixture B, which is a solution containing silica nanospheres used in the top layer solution. The silica sol (Nissan Chemical, IPA-ST-ZL) had the silica nanosphere concentration of 30 wt% and sphere size (diameter) distribution shown in **Fig. S3**, which is slightly larger than that specified by the manufacturer (between 70 nm and 100 nm). TEOS-derived SiO_2 composition was calculated to be 5 wt%, while the calculated silica composition was 5 wt%. Therefore, the calculated silica composition becomes 10 wt%, which is close to the measured value of 12 wt%.

Supplementary Note 6: Modelling of coating performance on a large-scale receiver

The spectral directional absorptance and spectral hemispherical emittance of the coatings are assumed temperature independent, as the temperature-dependence of the intrinsic optical properties of the coating are out of the scope of this study (no access to suitable equipment). The following methods are implemented in Step (1) *simulations at the pipe length scale* under the method "Evaluation of the coating performance on a high-temperature receiver" (see Methods).

Solar-weighted directional absorptance. The spectral directional hemispherical absorptance measurements obtained from spectrophotometry are integrated into a solar-weighted directional absorptance value considering the typical spectral distribution of sunlight, as detailed in Eq. (3). The Incidence Angle Modifier (IAM) model from Martin & Ruiz[23] was modified with the exponent c in Eq. (S1) and used to fit the solar weighted directional absorptance using the Nelder-Mead algorithm as implemented in SciPy.[24,25]

$$\alpha(\theta) = \alpha(\theta = 0)\frac{1 - e^{\left(-\cos(\theta)^c / a_r\right)}}{1 - e^{(-1/a_r)}}. \tag{S1}$$

The resulting fitted solar-weighted direction absorptance for the four coating cases evaluated are given in **Fig. N11a**.

Temperature-weighted emittance. The emittance is assumed Lambertian. While the spectral normal emittance itself is assumed temperature independent, the spectral emissive power of the blackbody is temperature dependent and influences the temperature-weighted emittance of the coatings evaluated. The temperature dependent emittance ε_{emi} is fitted to the following equation using the Nelder-Mead algorithm, as illustrated in **Fig. N11b**, and then implemented in the ray-tracing software.

$$\varepsilon_{\text{emi}}(T) = a - be^{c\frac{T - T_0}{\Delta T}}. \tag{S2}$$

Reflection model. In both the solar and thermal emission spectral regions, the coating surface is assumed to behave as a Lambertian surface for outgoing reflected radiation.

Receiver panel effective directional absorptance. An elementary volume of a receiver panel model is set-up to evaluate the radiative performance of tube banks in large scale receivers. This elementary volume is bounded on four sides by periodic boundary conditions to effectively approximate the impact of the rest of the panel on each individual volume as shown in **Fig. N12a**. The central pipe measures the angular dependent absorptance and two half-pipes are included to efficiently consider the influence of the rest of the bank. The insulation board at the back of the panel element is assumed

Lambertian with a diffuse total absorptance of 40%. The directional radiative properties of the coating are applied to the cylindrical pipe surfaces and the simulation run to evaluate the effective absorptance of the bank in all directions of the incident hemisphere.

Receiver panel effective thermal emittance. Assuming the emittance to be diffuse, the effective thermal emittance of the panels can be approximated based on geometrical considerations. Neglecting the small gap between pipes, the effective thermal emittance of infinite adjacent cylindrical pipes[26] is given by

$$\varepsilon_{\text{emi,panel}}(T) = \frac{\pi}{\frac{2}{\varepsilon_{\text{emi}}(T)} + \pi - 2}. \tag{S3}$$

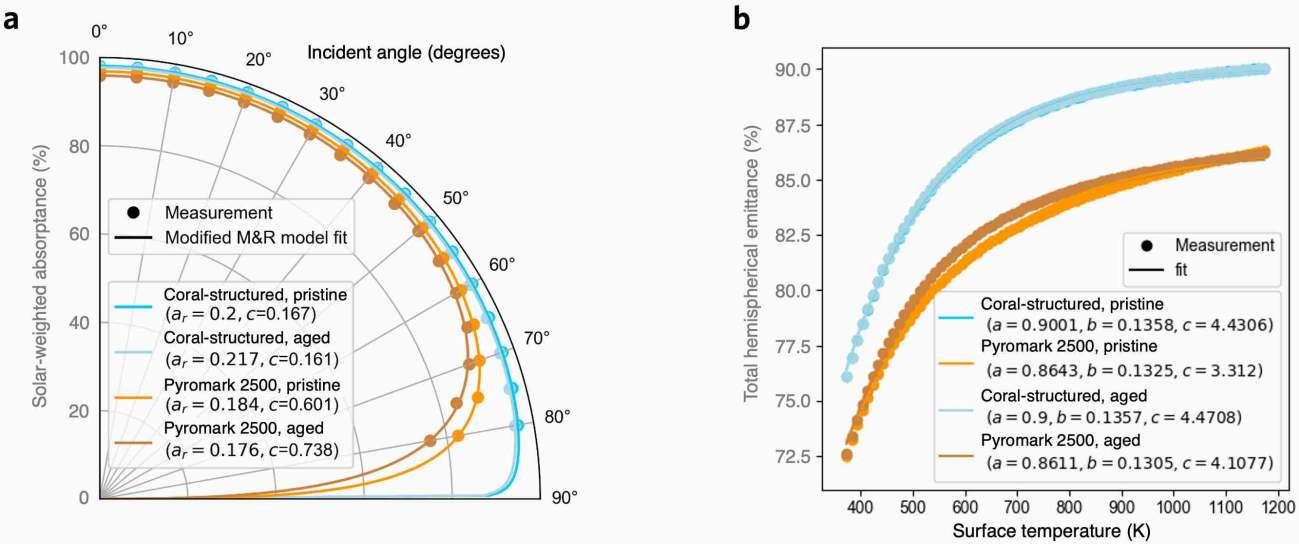

Fig. N11 | Curve fitting for optical properties used in the CST power plant-level modelling. The markers indicate measured values, whereas solid lines indicate fitted values, whose coefficients are indicated in the legend. **a**, Angular solar-weighted absorptance for the coral-structured coating and Pyromark in pristine condition and after ageing at 800°C for 1000 h; see **Fig. S8** for reported measured values. **b**, Total hemispherical emittance (temperature-weighted emittance) for the coral-structured coating and Pyromark in pristine condition and after ageing at 800°C for 1000 h; see **Fig. S11** for estimated values of total hemispherical emittance from measured spectral directional emittance. As in Ref. [4], the ratio of total hemispherical emittance to spectral directional emittance is assumed to be 0.94.

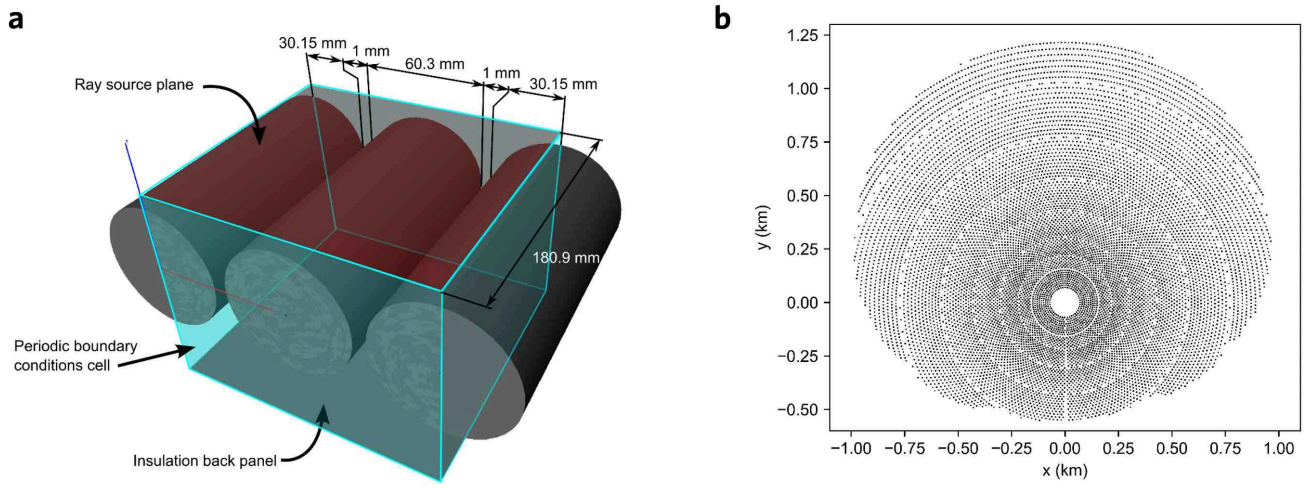

Fig. N12 | Geometry in tube-level and power-plant-level length scales. **a**, Illustration of the elementary volume of the receiver panel. The central pipe is separated from adjacent pipes by a 1 mm gap, necessary for manufacturing purposes. One pipe diameter of distance to the insulation board was set at the back of the panel (the image is an illustration with exaggerated dimensions for visibility). The length of the panel element is two pipe diameters plus two gaps. **b**, Heliostat field layout.

The following methods are implemented in Step (2) *simulations at the CST power plant length scale* under the method "Evaluation of the coating performance on a high-temperature receiver" (see Methods).

Field and receiver design. The field layout, composed of 11,373 heliostats, is situated in Daggett, California, USA, was determined using SolarPILOT from the National Renewable Energy Laboratory (NREL)[27] and is presented in **Fig. N12b**. Each heliostat is constituted of a single 7.07 m by 7.07 m square mirror facet, spherically curved at slant range to the mid-height of the receiver that sits on the top of a 150 m tower. The heliostats adopt an azimuth-elevation tracking actuation, have an overall statistical optical error of 1.5 mrad and a solar weighted absorptance of 90%, including some allowance for soiling and other performance degradation mechanisms. The 350 MWth receiver configuration is compatible with the United States Department of Energy (DOE) Gen3 and Australian Solar Thermal Research Institute (ASTRI) programs targets and operates between 520°C and 740°C. The heat-transfer fluid used in this receiver is liquid sodium which is compatible with such high temperatures and has interesting heat-transfer properties and the receiver is assumed to be built in Inconel 740H. The main design characteristics of the receiver are presented in **Fig. N13**.

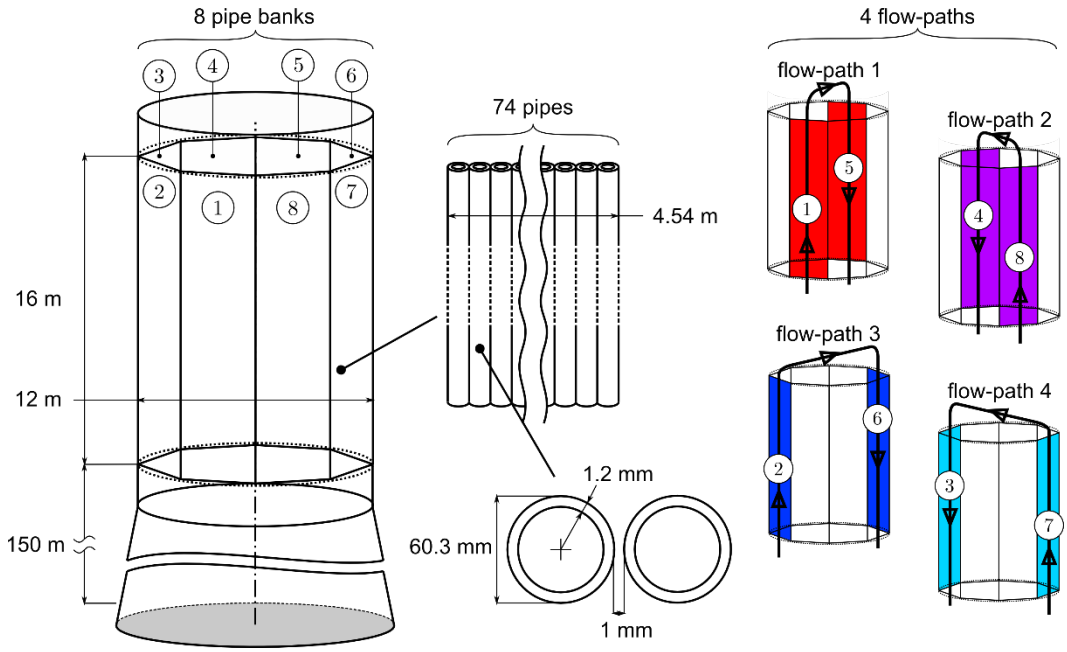

Fig. N13 | Design summary and main dimensions of receiver pipe banks and flow-paths. Design summary with the main dimensions and arrangement of the 8 pipe banks and summary of the 4 flow-paths.

In the power plant level simulation, the receiver bank aperture, i.e. external flat surface tangent to the pipe banks, is discretized into 34 by 10 rectangular mesh elements and the radiative energy falling into each one of these rectangular elements is used as a source term for the flow-path energy balance model.

The receiver simulations presented in the main manuscript are realized at equinox solar noon (azimuth 180°, elevation 55.08°) for a Direct Normal Irradiance (DNI) of 980 W m^{-2}. The sunshape model adopted is the Buie sunshape, assuming a circumsolar ratio of 2%, compatible with mostly clear sky conditions. Simulations are run for 10 million rays in Solstice, a ray-tracing code dedicated to CST power plant simulation making use of a range of Monte Carlo ray tracing (MCRT) simulation acceleration techniques.

Energy balance model presentation. The solution of the energy, mass and momentum balance in the receiver proceeds as follows:

1. Radiation incident on the aperture of the receiver panels is obtained from the ray-tracing simulation of the heliostat field and receiver at equinox solar noon, using a direct normal irradiance of 1000 W m^{-2} and a circumsolar ratio of 2%.
2. The directional input into each receiver panel is mapped onto the effective directional absorptance to determine the absorbed radiation on each panel element and corresponding receiver flow-path element.

3. The flow-path model iteratively solves energy mass and momentum balances on the pipe banks, headers and connections based on finite differences approximations until variation in external wall temperatures between two iterations falls below 0.01%. In this model, thermal emissions are evaluated based on the temperature dependent effective thermal emittance of the receiver panels and mixed convective loss evaluated using the Siebers and Kraabel correlation[28] assuming a typical wind speed of 5 m s^{-1} for the site of concern. The incompressible liquid sodium thermophysical properties are obtained from Fink and Leibowitz[29] and pipe internal heat transfer coefficient obtained using the Skupinski-Tortel-Vautrey correlation.[30]

This model is coded in Python language and is made available online on the collaborative development platform GitHub[31].

Supplementary Note 7: On the practical limits of the hierarchical structure

The performance of our hierarchical sunlight absorber coating can be constrained by its thermal barrier, which refers to the temperature difference between the tube–coating and the coating–air boundary, as shown in **Fig. N14**. Note that, for an irradiated coating, the external surface (coating–air boundary) is hotter than its internal surface (tube–coating boundary). The thermal barrier is then proportional to the heat conduction path, i.e. coating thickness (t_{coat}), and inversely proportional to the heat conduction rate, i.e. thermal conductivity (k_{coat}). If the effective thickness of the coating becomes very large due to the added hierarchical features (or its thermal conductivity is very low), then a very large temperature difference through the coating may occur. As the temperature of the heat transfer fluid (HTF) passing through the tubes is regulated, e.g. by varying its flow rate, then the large temperature difference yields a large external surface temperature that results in large convective and radiative heat losses[14].

Preliminary measurements indicate that the thermal conductivity of our coating is about 0.89 W m^{-1} K^{-1}. This is at the lower end of the range of thermal conductivity values reported in the literature for Pyromark 2500, with reported values ranging from 0.6 to 6.26 W m^{-1} K^{-1} (Ref. [32]). The low thermal conductivity of our coating can be attributed to the air gaps in the macro- and micro-scale levels. Although a reduction in thermal conductivity increases the thermal barrier, our receiver modelling (Supplementary **Note 6**) indicates that the effect of thermal conductivity on receiver thermal

efficiency is marginal, as shown in **Fig. N15a**. Here, the receiver thermal efficiency only decreases by 0.15% when reducing the thermal conductivity of the coatings from 6.26 W m^{-1} K^{-1} (upper value of Pyromark[32]) to 0.89 W m^{-1} K^{-1} (our coating) when assuming an absorptance of 98%, emittance of 91%, and coating thickness of 40 μm. Multiple cross-section measurements of our coral-structured coating (Supplementary **Note 3**) show the coating thickness to be 37 μm in average with a standard deviation of 15 μm. The modelling is conducted for different sun positions, with summer yielding the largest receiver thermal efficiency.

To predict the practical limitations for coating thickness, further modelling was conducted based on the large-scale solar thermal power plant. Here, we implement the measured thermal conductivity of our coating of 0.89 W m^{-1} K^{-1}, yielding the results shown in **Fig. N15b**. Interestingly, during most daylight hours (until noon ±4 h), a coating thickness greater than 200 μm yields excessive temperatures in the coating that invalidate any numerical solution. Hence, the practical limit for the thickness of our coral-structured coating is expected to be ca. 200 μm, much larger than the 37 μm (average) produced in this study. Note that the most stringent condition was found for the summer noon + 2 h (not noon as could be expected), which is caused by higher fluxes on the banks of the receiver that are positioned closer to the end of the flow-path (see **Fig. N13**). **Figure 15Nb** also shows that the thermal efficiency of the receiver decreases almost linearly with the coating thickness. This is due to an increase in external surface temperature that amplifies the thermal losses. For a thickness of less than 40 μm, the penalty in solar thermal efficiency is less than 1% compared to an infinitively thin coating.

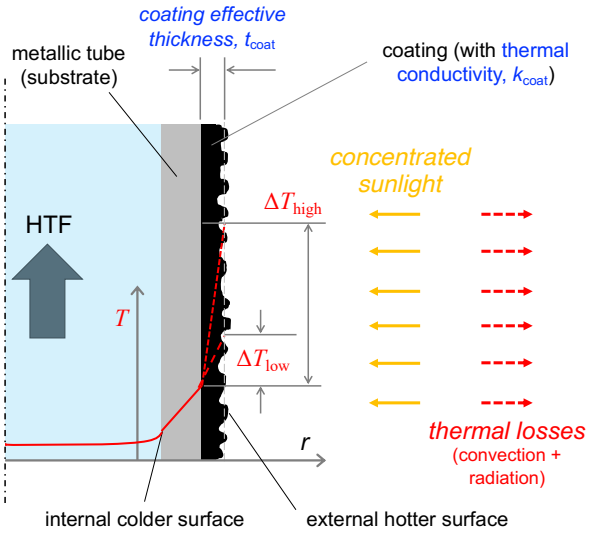

Fig. N14 | Schematic depicting the thermal barrier in a high-temperature sunlight absorber. The coating thermal barrier refers to the temperature difference through the coating. As the heat transfer fluid (HTF) is kept at a constant temperature, this results in an increase of external surface temperature that could drastically decrease the thermal efficiency of the receiver due to large thermal losses. The thermal barrier is directly proportional to the coating thickness and inversely proportional to the coating thermal conductivity.

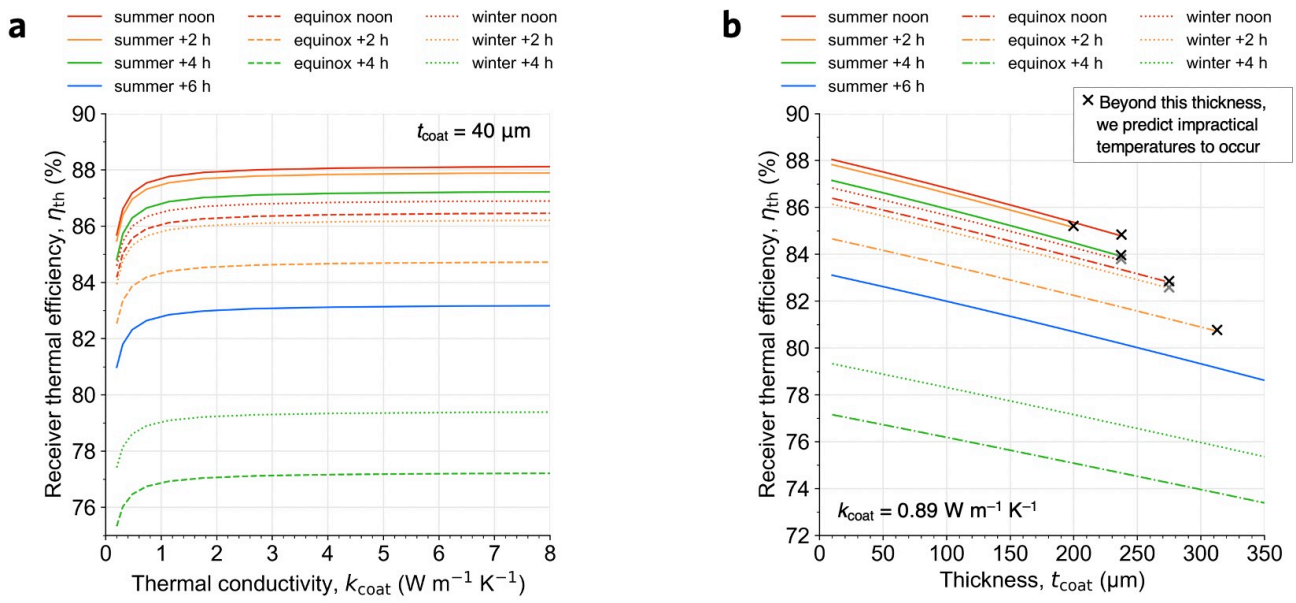

Fig. N15 | Modelling results showing the effect of thermal barrier on receiver thermal efficiency. The thermal barrier is detrimental to the receiver thermal efficiency when the thermal conductivity becomes small, or the coating thickness becomes large. **a**, Receiver thermal efficiency as a function of the coating thermal conductivity when its effective thickness is 40 µm. **b**, Receiver thermal efficiency as a function of the coating effective thickness when its thermal conductivity is 0.89 W m^{-1} K^{-1}. Beyond the thickness indicated by cross, impractically high temperatures in the receiver were found. Thus, this thickness could serve as a practical limit of the coating.

It is worth mentioning that, although the receiver thermal efficiency is larger in winter than in the equinox (**Figs. N14–N15**), the DNI in winter is lower than in the equinox. Therefore, the equinox yields a larger solar thermal energy output than in winter. The receiver thermal efficiency depends on a combination of optical and thermal factors, such as the number of aiming heliostats and the resulting flux distributions.

Supplementary References

1. Zeng, Z. *et al.* Effect of element diffusion through metallic networks during oxidation of Type 321 stainless steel. *J. Mater. Eng. Perform.* **23**, 1247–1262 (2014).
2. Huang, X. *et al.* Oxidation behavior of 316L austenitic stainless steel in high temperature air with long-term exposure. *Mater. Res. Express* **7**, (2020).
3. Torres, J. F., Ellis, I. & Coventry, J. Degradation mechanisms and non-linear thermal cycling effects in a high-temperature light-absorber coating. *Sol. Energy Mater. Sol. Cells* **218**, 110719 (2020).
4. Ho, C. K. *et al.* Characterization of Pyromark 2500 paint for high-temperature solar receivers. in *Proceedings of the ASME 2012 6th International Conference on Energy Sustainability* 91374 (2012).
5. González de Arrieta, I. *et al.* Infrared emissivity of copper-alloyed spinel black coatings for concentrated solar power systems. *Sol. Energy Mater. Sol. Cells* **200**, 109961 (2019).
6. Ambrosini, A., Boubault, A., Ho, C. K., Banh, L. & Lewis, J. R. Influence of application parameters on

stability of Pyromark® 2500 receiver coatings. *AIP Conf. Proc.* **2126**, 030002 (2019).

7. Noč, L. *et al.* High-solar-absorptance CSP coating characterization and reliability testing with isothermal and cyclic loads for service-life prediction. *Energy Environ. Sci.* **12**, 1679–1694 (2019).
8. Harzallah, R., Larnicol, M., Leclercq, C., Herbein, A. & Campana, F. Development of high performances solar absorber coatings. *AIP Conf. Proc.* **2126**, (2019).
9. Rubin, E. B., Chen, Y. & Chen, R. Optical properties and thermal stability of Cu spinel oxide nanoparticle solar absorber coatings. *Sol. Energy Mater. Sol. Cells* **195**, 81–88 (2019).
10. Rubin, E. B., Shin, S., Chen, Y. & Chen, R. High-temperature stable refractory nanoneedles with over 99% solar absorptance. *APL Mater.* **7**, (2019).
11. Caron, S. *et al.* Forty shades of black: A benchmark of high temperature sprayable black coatings applied on Haynes 230. *AIP Conf. Proc.* **2303**, (2020).
12. Chung, D., Hutchins, N., Schultz, M. P. & Flack, K. A. Predicting the Drag of Rough Surfaces. *Annu. Rev. Fluid Mech.* **53**, 439–471 (2021).
13. Bechert, D. W., Bruse, M., Hage, W., Van Der Hoeven, J. G. T. & Hoppe, G. Experiments on drag-reducing surfaces and their optimization with an adjustable geometry. *J. Fluid Mech.* **338**, 59–87 (1997).
14. Torres, J. F., Ghanadi, F., Wang, Y., Arjomandi, M. & Pye, J. Mixed convection and radiation from an isothermal bladed structure. *Int. J. Heat Mass Transf.* **147**, 118906 (2020).
15. Blossey, R. Self-cleaning surfaces — virtual realities. *Nat. Mater.* **2**, 301–306 (2003).
16. Chamberlain, J. A. & Graus, R. R. Water-flow and hydromechanical adaptations of branched reef corals. *Bull. Mar. Sci.* **25**, 112–125 (1975).
17. Duckworth, A., Giofre, N. & Jones, R. Coral morphology and sedimentation. *Mar. Pollut. Bull.* **125**, 289–300 (2017).
18. Dean, B. & Bhushan, B. Shark-skin surfaces for fluid-drag reduction in turbulent flow: A review. *Philos. Trans. R. Soc. A Math. Phys. Eng. Sci.* **368**, 4775–4806 (2010).
19. Anderson, W. & Meneveau, C. Dynamic roughness model for large-eddy simulation of turbulent flow over multiscale, fractal-like rough surfaces. *J. Fluid Mech.* **679**, 288–314 (2011).
20. Anjum, A. S., Sun, K. C., Ali, M., Riaz, R. & Jeong, S. H. Fabrication of coral-reef structured nano silica for self-cleaning and super-hydrophobic textile applications. *Chem. Eng. J.* **401**, 125859 (2020).
21. Nofz, M., Dörfel, I., Sojref, R. & Saliwan Neumann, R. Microstructure of Bare and Sol–Gel Alumina-Coated Nickel-Base Alloy Inconel 625 After Long-Term Oxidation at 900 °C. *Oxid. Met.* **91**, 395–416 (2019).
22. Coventry, J. & Burge, P. Optical properties of Pyromark 2500 coatings of variable thicknesses on a range of materials for concentrating solar thermal applications. *AIP Conf. Proc.* **1850**, 030012 (2017).
23. Martin, N. & Ruiz, J. M. Calculation of the PV modules angular losses under field conditions by means of an analytical model. *Sol. Energy Mater. Sol. Cells* **70**, 25–38 (2001).
24. Nelder, J. A. & Mead, R. A simplex method for function minimization. *Comput. J.* **7**, 308–313 (1965).
25. Jones, E., Oliphant, T., Peterson, P. & others. SciPy: Open source scientific tools for Python. (2001).
26. Holman, J. P. *Heat Transfer*. (McGraw-Hill, 1989).
27. Wagner, M. J. & Wendelin, T. SolarPILOT: A power tower solar field layout and characterization tool. *Sol. Energy* **171**, 185–196 (2018).
28. Siebers, D. L. & Kraabel, J. S. *Estimating convective energy losses from solar central receivers*. (Sandia

National Laboratories, 1984).

29. Fink, J. K. & Leibowitz, L. *Thermodynamic and transport properties of sodium liquid and vapor*. (Argonne National Lab., 1995).

30. Skupinski, E., Tortel, J. & Vautrey, L. Determination des coefficients de convection d'un alliage sodium-potassium dans un tube circulaire. *Int. J. Heat Mass Transf.* **8**, 937–951 (1965).

31. Asselineau, C.-A. Tracer: a Pythonic ray-tracing package with solar energy focus. (2021). Available at: https://github.com/casselineau/Tracer.

32. Boubault, A., Claudet, B., Faugeroux, O. & Olalde, G. Aging of solar absorber materials under highly concentrated solar fluxes. *Sol. Energy Mater. Sol. Cells* **123**, 211–219 (2014).